J. Fluid Mech. (2009), *vol.* 640, *pp.* 305–342.
doi:10.1017/S002211200999139X

Behaviour of an air-assisted jet submitted to a transverse high-frequency acoustic field

F. BAILLOT[1]†, J.-B. BLAISOT[1], G. BOISDRON[1,2] AND C. DUMOUCHEL[1]

[1]CORIA, UMR 6614, CNRS, Université et INSA de Rouen, BP 12, 76801 Saint Etienne du Rouvray, France

[2]Altran AIT, 2 Rue Paul Vaillant Couturier, 92300 Levallois-Perret, France

(Received 17 July 2008; revised 14 July 2009; accepted 27 July 2009)

Acoustic instabilities with frequencies roughly higher than 1 kHz remain among the most harmful instabilities, able to drastically affect the operation of engines and even leading to the destruction of the combustion chamber. By coupling with resonant transverse modes of the chamber, these pressure fluctuations can lead to a large increase of heat transfer fluctuations, as soon as fluctuations are in phase. To control engine stability, the mechanisms leading to the modulation of the local instantaneous rate of heat release must be understood. The commonly developed global approaches cannot identify the dominant mechanism(s) through which the acoustic oscillation modulates the local instantaneous rate of heat release. Local approaches are being developed based on processes that could be affected by acoustic perturbations. Liquid atomization is one of these processes. In the present paper, the effect of transverse acoustic perturbations on a coaxial air-assisted jet is studied experimentally. Here, five breakup regimes have been identified according to the flow conditions, in the absence of acoustics. The liquid jet is placed either at a pressure anti-node or at a velocity anti-node of an acoustic field. Acoustic levels up to 165 dB are produced. At a pressure anti-node, breakup of the liquid jet is affected by acoustics only if it is assisted by the coaxial gas flow. Effects on the liquid core are mainly due to the unsteady modulation of the annular gas flow induced by the acoustic waves when the mean dynamic pressure of the gas flow is lower than the acoustic pressure amplitude. At a velocity anti-node, local nonlinear radiation pressure effects lead to the flattening of the jet into a liquid sheet. A new criterion, based on an acoustic radiation Bond number, is proposed to predict jet flattening. Once the sheet is formed, it is rapidly atomized by three main phenomena: intrinsic sheet instabilities, Faraday instability and membrane breakup. Globally, this process promotes atomization. The spray is also spatially organized under these conditions: large liquid clusters and droplets with a low ejection velocity can be brought back to the velocity anti-node plane, under the action of the resulting radiation force. These results suggest that in rocket engines, because of the large number of injectors, a spatial redistribution of the spray could occur and lead to inhomogeneous combustion producing high-frequency combustion instabilities.

Key words: acoustics, aerosols/atomization, multiphase

† Email address for correspondence: baillot@coria.fr

1. Introduction

Ever since the early development of liquid rocket engines in the 1940s, unexpected combustion instabilities have affected the operation of engines in almost all the propulsion system programmes. These instabilities are characterized by pressure oscillations of three types: (i) chugging instabilities (low frequency), (ii) buzzing instabilities (intermediate frequency roughly lower than a few kilohertz) and (iii) screaming or acoustic instabilities (high frequency roughly higher than 1 kHz). Types (i) and (ii) involve the entire combustion system, including supply tanks, propellant feed lines, combustor and exhaust elements. In the third type, the instabilities couple with the resonant transverse modes of the chamber. The latter instabilities, by increasing heat transfer, often lead to the destruction of the engine. Harrje & Reardon (1972) carefully summarized research carried out on the subject during the 1960s and early 1970s, while Anderson & Yang (1995) proposed a more recent review of the state of the art in the 1990s.

As formally identified by Rayleigh, combustion instability amplifications occur when heat release is in phase with pressure fluctuations. If the acoustic pressure modulates the rate of heat release, a feedback loop takes place. The system thus becomes unstable as soon as the pressure wave amplifications cannot be counterbalanced by acoustic losses in the chamber. To control engine stability, the mechanisms leading to the modulation of the local instantaneous rate of heat release must be understood (Candel, Huynh & Poinsot 1996, pp. 83–112).

Global approaches such as the sensitive time lag concept are commonly developed to predict the whole energetic response of the chamber, but these approaches cannot identify the dominant mechanism(s) through which acoustic oscillations modulate the local instantaneous rate of heat release. Identifying these mechanisms is crucial in constructing effective predictive codes; so local approaches are being developed based on processes that acoustic perturbations could impact on.

Liquid atomization is one of these processes. Indeed, under typical operating conditions in rocket engines, acoustic pressure fluctuations can reach 10 % of the average chamber pressure. Thus, the whole atomization process can be affected by such an intense acoustic field, especially during the transitory phases when their nominal state has not yet been attained.

There is little work treating the response of a liquid jet to acoustic perturbations. As the present work focuses on the impact of a transverse acoustic field, the effect of a longitudinal acoustic field (e.g. see Sujith 2005 for an air-assisted spray) is not considered here. In the literature, works devoted to fluid systems placed at a pressure node of a transverse acoustic field focused essentially on the response of a small droplet (ultrasonic waves), seldom on the response of a free jet (ultrasonic and high-frequency waves) and even more seldom on the response of a coaxial jet (high-frequency waves). First, Buffum & Williams (1967) studied how a transverse acoustic field with an acoustic level greater than 140 dB influences a non-assisted turbulent liquid jet placed at a pressure node. They found that the jet was displaced in the direction of the transverse acoustic field at the forcing frequency. The amplitude of the displacement increased with the acoustic level and was approximately 10 times greater than what would be predicted when using the steady-flow drag coefficient for a solid cylinder. This phenomenon was interpreted as being caused by a drag enhancement resulting from the non-quasi-steady gas flow around the jet. Above 160 dB, the jet began to be atomized at twice the acoustic frequency. Hoover *et al.* (1991) observed a jet flattened like a sheet under the action of high-frequency acoustic perturbations, if the acoustic level was high enough. The flattening occurred perpendicular to the acoustic direction.

These authors suggested that the flattening arose from a velocity coupling mechanism similar to the deformation induced by the impact of two opposite transverse steady gas flows on a round jet. However, the two flow configurations they compared did not fall in the same range of Weber numbers. So, even though the authors found similar tendencies, the results suggest that the physical mechanisms involved in the flattening of the jet are quite different in the two experiments. A similar flattening is noted in the results reported by Chehroudi & Talley (2002) for a free liquid jet of nitrogen introduced into a chamber at room temperature under sub- or supercritical pressures (see also Oschwald *et al.* 2006). Even though no physical explanations were given, the authors mentioned that the impact of the acoustic waves on the jet structure was strong at subcritical pressures, strongest at near-critical pressures and weakest at supercritical pressures. To complete this high-pressure chamber study, Davis & Chehroudi (2006) extended it to a shear coaxial jet still constituted of a central liquid jet of nitrogen, with the addition of an annular gaseous nitrogen coflow. But no flattening phenomenon was observed by the authors. This feature will be highlighted in § 5.2 through the results presented here.

A greater number of studies are found in the literature for the domain of ultrasonic waves. Flattening of the jet is also observed in ultrasonic standing-wave atomization (USWA), a process used to produce spherical metal powders from a non-assisted jet of melt metal crossing a high-amplitude transverse standing acoustic field (a few tens of kilohertz). Andersen, Hansmann & Bauckage (1996) and Bauckage *et al.* (1996) gave a heuristic explanation based on the work of Lee, Anilkumar & Wang (1991) concerning the deformation and the subsequent atomization of a single droplet. These authors invoked the effect of the radiation pressure to explain the deformation of the jet.

Reipschläger *et al.* (2002) and Lessmann (2004) carried out numerical simulations able to reproduce the flattening of a round jet into a sheet under the USWA conditions. Lessmann explained that the flattening of the liquid jet results from the deviation of the acoustic streamlines in the vicinity of the jet. This induces a maximum suction tension in the pressure node plane, able to stretch the liquid in this plane.

Finally these results indicate that a liquid jet or a drop placed at a pressure node may be either deviated or flattened, depending on whether a physical threshold, not identified by the authors, is exceeded.

In the present paper the effect of transverse acoustic perturbations on a coaxial air-assisted jet is studied experimentally. Their action appears as a consequence of nonlinear acoustic effects, involving the local radiation pressure distribution and/or the resulting radiation pressure force. The liquid jet is placed either at a pressure anti-node or at a velocity anti-node of the acoustic field. Characteristics of both the continuous and dispersed phases are quantified. Acoustic levels up to 165 dB are produced (using the standard reference pressure of 2×10^{-5} Pa). Such high acoustic levels are representative of those leading to the occurrence of high-frequency instabilities in rocket engines. Here, the action of the local radiation pressure distribution which flattens the coaxial jet at a pressure node is clearly shown, and also the action of the resulting radiation pressure force which can drive the movement of drops towards the pressure node.

Flow conditions are indicated in terms of non-dimensional numbers, i.e. the gaseous Weber number $We = (\rho_g U_g^2 D_l)/\sigma$, the liquid Reynolds number $Re_l = (D_l U_l)/\nu_l$, the momentum flux ratio $J = (\rho_g U_g^2)/(\rho_l U_l^2)$, the Ohnesorgue number $Oh = \mu_l/\sqrt{\rho_l \sigma D_l}$ and the Mach number $Ma = U_g/c$. Here, ρ_g and ρ_l stand for the gaseous and liquid densities; U_g and U_l represent the gas and the liquid flow-rate velocities; σ is the

surface tension of the liquid; ν_g is the gas kinematic viscosity; μ_l is the liquid dynamic viscosity; and c is the speed of sound in the gas. The gaseous Weber number We (based on ρ_g and U_g) is chosen instead of the relative gaseous Weber number We_{rel} (based on ρ_g and $|U_g - U_l|$) commonly used in the literature. The reason is that in a (We_{rel}, Re_l) mapping, results overlap for conditions $U_g < U_l$ and $U_l < U_g < 2U_l$.

The experimental set-up is introduced in the next section. The atomization regimes observed without acoustic excitations and the characterization of the acoustic field generated in our experiments are then presented. The two subsequent sections are related to results obtained when the injection is performed at a pressure anti-node or at a velocity anti-node respectively. A physical threshold based on a modified acoustic Bond number, the radiation Bond number, is proposed to predict when jet flattening occurs at a pressure node. It extends the traditional definition of the Bond number, used in the ultrasonic works. Enhancement of atomization process is plainly quantified; in particular the different phenomena, the Faraday instability, sheet instabilities and membrane disintegration, are carefully described. The duality between the unsteadiness of the annular gas flow and the mean nonlinear behaviour of the liquid–gas system is revealed at a pressure anti-node. A conclusion ends this paper.

2. Experimental set-up

2.1. *Injection and acoustic cavity*

The injector reproduces a rocket engine injector used by ONERA on the French bench 'Mascotte' (see Rey 2004). The liquid used is water, and the gas flowing around the liquid jet is air. The experiments are performed at atmospheric pressure. Details of the injector's internal design are shown in figures 1(a) and 1(b). Water flows through a cylindrical tube 100 mm long with an 8 mm internal diameter. The diameter reduces to 5 mm along the last 20 mm of the tube. On the last millimetre of the tube, the nozzle diverges with a half-angle of 6°, leading to a sharp-edged exit nozzle of diameter $D_l = 6$ mm. Thus, a quite null thickness separates the two fluids in the exit plane (see figure 1b). The air is introduced by two apertures facing each other at the top of the injector and flows into a large quiescent chamber containing honeycombs to break up large eddies. This chamber is followed by a convergent passage whose outer exit diameter is $D_g = 8$ mm, leading to an annular airflow of width $e = 1$ mm in the exit plane. Both air and water flows are controlled by mass flow metres. Maximum flow-rate velocities are 175 and 0.8 m s^{-1} for the gas and the liquid, respectively. Consequently, the experimental set-up covers the following ranges of the non-dimensional parameters:

$$\left.\begin{array}{l} 0 \leqslant We \leqslant 3300, \\ 0 \leqslant Re_l \leqslant 6000, \\ 0 \leqslant J \leqslant 4000, \\ Oh = 1.3 \times 10^{-3}, \\ Ma \leqslant 0.5. \end{array}\right\} \tag{2.1}$$

In order to generate an intense acoustic standing wave, a semi-opened cavity is used (see figure 1c). It consists of two parallel and vertical steel plates and a PVC roof. The injector is mounted such that its exit plane coincides with the inner surface of the roof. The two vertical plates are $L_c = 360$ mm apart in order to optimize the acoustic field at the frequency $f = 1000$ Hz. A maximum sound pressure level (SPL) of 165 dB is

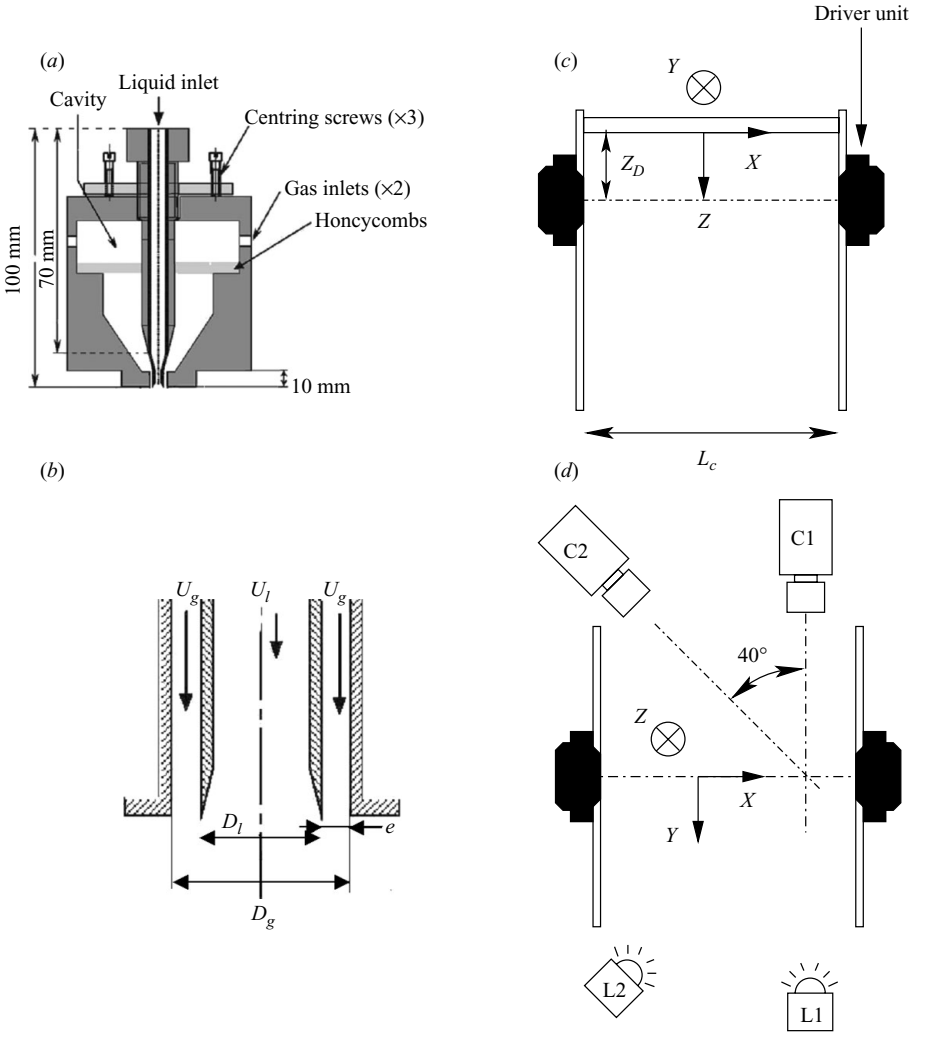

FIGURE 1. Experimental set-up: (*a*) global view of the coaxial injector, (*b*) details of the injector nozzle exit, (*c*) side view of the acoustic resonant cavity, (*d*) top view of the acoustic cavity. Configurations of the camera (C) and the light source (L) for the front view (1) and side view (2) used for the visualization of the jet are also indicated.

thus reached in the cavity. The reference frame (O, $\boldsymbol{X}$, $\boldsymbol{Y}$, $\boldsymbol{Z}$) is introduced to describe the position in the cavity; O is the centre of the inner surface of the roof; $\boldsymbol{X}$ is the horizontal axis perpendicular to the steel plates; and $\boldsymbol{Z}$ is the descending vertical axis. Two Beyma CP-850Nd driver units facing each other produce the acoustic field. They are centred on the steel plates ($Y = 0$) at $Z = Z_D = 82.5$ mm. These driver units are supplied in phase by a sine-wave signal generator, driven by an OROS OR36 analyzer, and a MACKIE M800 amplifier.

2.2. *Flow visualization and characterization*

The liquid jet was visualized through a backlight arrangement. Still images were recorded with a Kappa DX2N camera (8 bits, 1380 × 1024 pixels, 3 images s^{-1}), and

time-resolved image sequences were obtained with a Phantom v9.0 camera (8 bits, 1200 × 1632 pixels at 1000 images s^{-1} and 480 × 960 pixels at 3600 images s^{-1}). A stroboscopic light source delivering flashes of 0.75 μs duration was used for still images. At least 30 still images were recorded for each operating condition. A 1500 W continuous light source was used for high-speed imaging. Front views and side views were performed for the visualization (see figure 1*d*). For the front views, the light source and the camera were aligned on the Y axis, and for the side views the optical axis of the camera formed an angle of 40° with the Y axis. A morphological image transformation was thus applied to side views to transpose images into what would have been obtained with an optical axis perpendicular to the Y axis. Visualizations resulting from this operation are called 'modified side views'.

The action of the acoustic field on the coflowing gas stream was visualized by the schlieren method. For this purpose, the injector was fed with CO_2 instead of air, and a high-speed Kodak 4540 camera recorded the jet evolution at a framing rate of 13 500 images s^{-1}, with an image resolution of 128 × 128 pixels.

Drop-size distributions were measured by a Malvern Spraytec 2500 spray sizing system. A focal length of 450 mm was chosen, allowing diameters ranging from 9 to 1040 μm to be measured.

The acoustic pressure modulation was measured by Bruel and Kjaer 4944 microphones. Pressure signals were sampled at 51.2 kHz by the OROS OR36 analyzer.

3. Background of the study

3.1. *Jet atomization regimes without acoustics*

Farago & Chigier (1992) proposed a classification of coaxial jet breakup regimes based on We_{rel} and Re_l. Hopfinger (1998) and Lasheras & Hopfinger (2000) pointed out that coaxial jet breakup regime categorization should account for at least three parameters, namely the gaseous Weber number We, the liquid Reynolds number Re_l and the momentum flux ratio J, named M in Hopfinger (1998) and Lasheras & Hopfinger (2000). Although they deplored a lack of experimental results giving the precise location of the different regime boundaries, they proposed the classification shown in figure 2, where the grey rectangle delimits the operating conditions covered by the present work.

Here, five breakup regimes have been identified according to the flow conditions, in the absence of acoustics. These regimes, presented in figures 3(*a*)–3(*e*), are the axisymmetric Rayleigh regime, the non-axisymmetric Rayleigh regime, the shear breakup regime, the membrane regime and the fibre-type regime, according to the designation proposed by Farago & Chigier (1992). The regimes are given above in the order of growing gas flow velocity. Characteristic lengths of the jets are introduced in these figures. The method of Otsu (1979) is applied to grey-level images (see figure 3) to obtain a binary version of them. The contour of the binary element attached at the nozzle exit is then determined. The breakup length is defined as the distance from the exit plane to the most downstream position of the contour. The same designations are used for quantities measured with instantaneous data and with corresponding mean data determined from about 30 images. Error bars, when indicated on the plots, correspond to plus/minus one standard deviation of the measurements. The boundaries found in the present work for the limits between the regimes are shown in figure 3(*f*). They are not perfectly superimposed on those found by Lasheras & Hopfinger (2000) for similar conditions. These discrepancies result from differences in

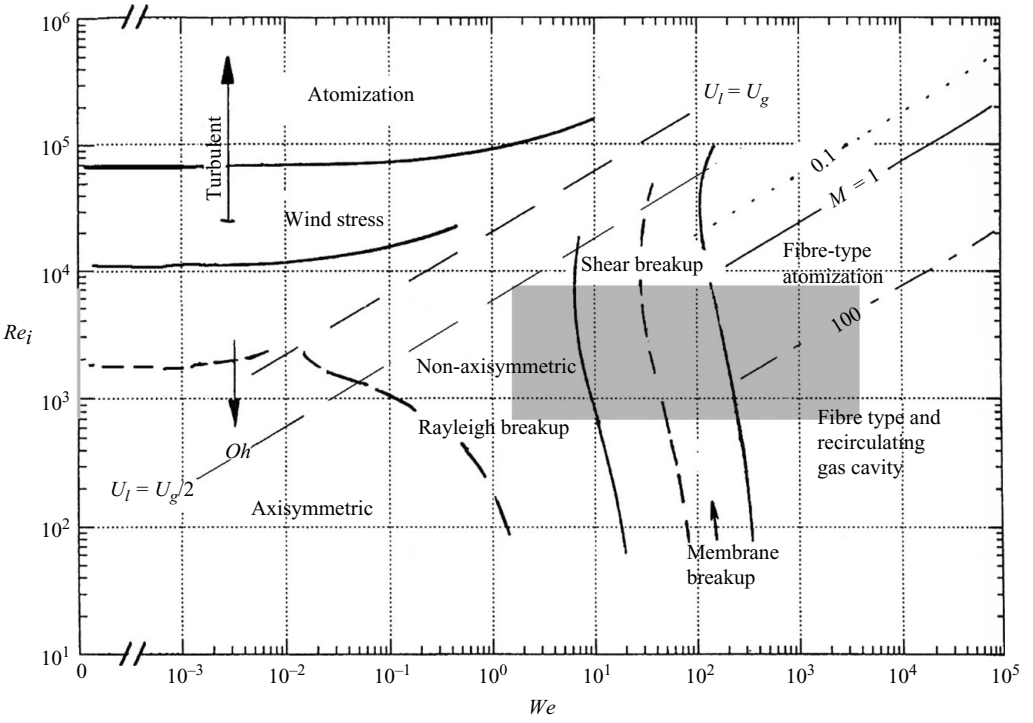

FIGURE 2. Diagram of the jet breakup regimes in the parameter space Re_l–We from Lasheras & Hopfinger (2000); M corresponds to the momentum flux ratio represented by J in the present paper; ▬ denotes the range of the present investigation.

nozzle geometries (annular gap, among others) and also in flow conditions (Ohnesorge number, vortex in the gas flow and the like).

The axisymmetric Rayleigh regime is bounded to the right by limits A and B in figure 3(*f*). Values of the Weber number corresponding to this boundary are higher than the value found by Lasheras & Hopfinger (2000). As seen in figure 3(*a*), for this regime the continuous part of the jet develops a Rayleigh capillary instability. Up to five sine-wave perturbations, characterized by the wavelength λ_R, can be observed before breakup occurs. It was found that $\lambda_R \simeq 3D_l$, which is lower than the value predicted by the linear theory, i.e. $\lambda_R = 4.51D_l$. Droplets of diameter D_G of the order of the liquid jet diameter are formed along the jet axis. The breakup length L^0_{bu} was found to increase with Re_l from $20D_l$ and reached asymptotically $45D_l$, with a concave curvature evolution (see Appendix A).

The non-axisymmetric Rayleigh breakup regime (figure 3*b*) is bounded by limits A and C in figure 3(*f*). This regime is also called 'first wind induced' in the literature (Lefebvre 1989). The continuous liquid core takes a sine-wave shape characterized by the wavelength λ_S. The breakup length is greatly reduced compared to the Rayleigh axisymmetric regime (see Appendix A). Four droplets of diameter $D_G \lesssim D_l$ are produced per wavelength, each of them being accompanied at most by one satellite droplet.

The shear breakup regime is bounded by limits B and C. A shear instability develops from the nozzle exit and deforms the liquid core symmetrically. These deformations, characterized by the shear wavelength λ_C (figure 3*c*), are amplified by the

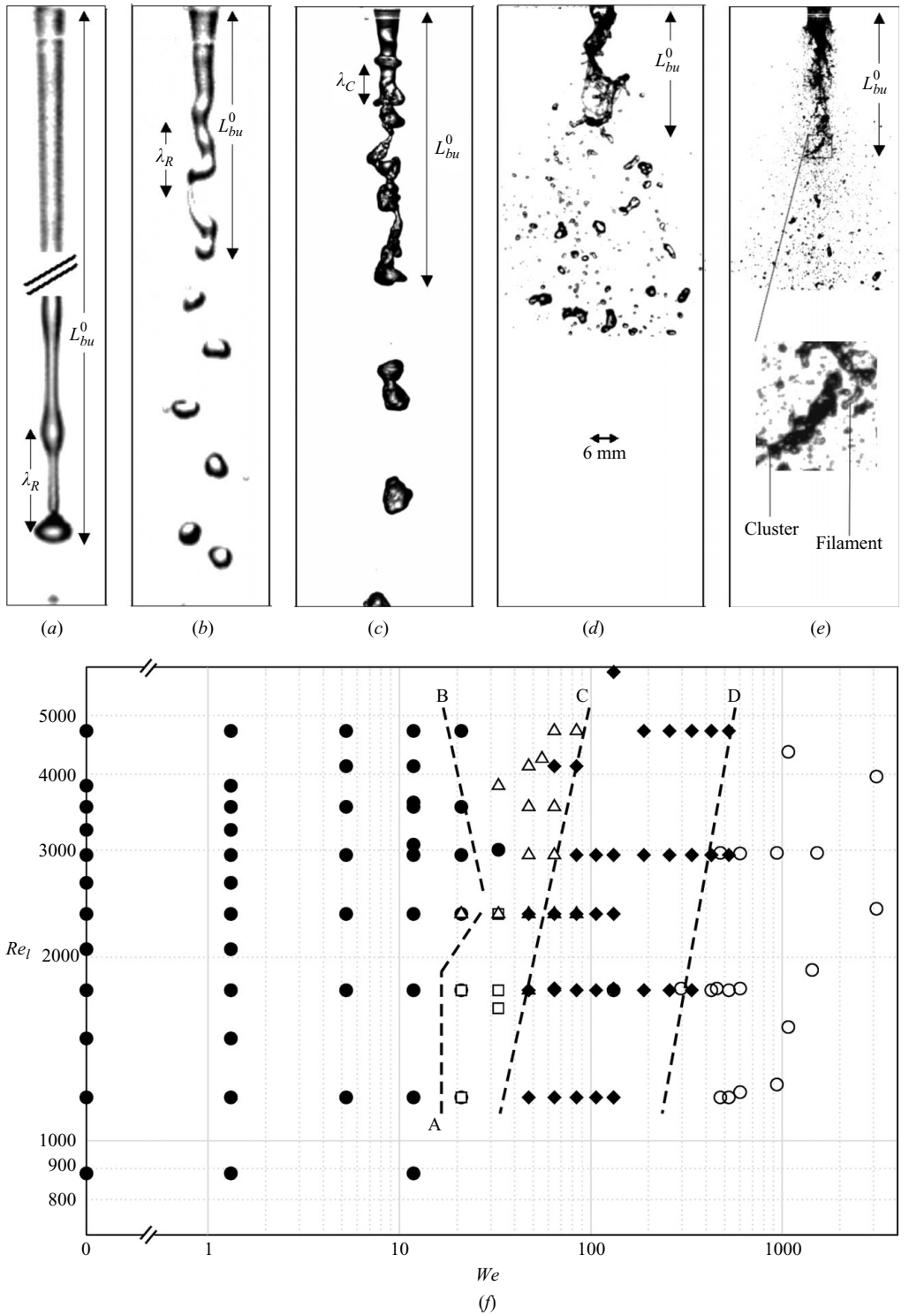

FIGURE 3. Breakup regimes observed without acoustics: (*a*) Rayleigh axisymmetric (●); (*b*) Rayleigh non-axisymmetric (□); (*c*) shear breakup (△); (*d*) membrane (◆); (*e*) fibre-type (○); (*f*) diagram of the jet breakup regimes from our experimental data.

Kelvin–Helmholtz rings created at the liquid–gas interface. The mean shear wavelength λ_C measured for the shear breakup regime ranges from $5e$ to $10e$. It decreases mainly with $Re_g^{-0.5}$, for Re_g ranging from 850 to 3000, as already observed by Marmottant (2001), who modelled the shear instability variation as an effect consecutive to the gas boundary layer developing from the nozzle exit. The amplification of the shear deformations leads to the formation of ligaments due to a secondary Rayleigh–Taylor transverse instability (see Raynal 1997; Villermaux 1998; Marmottant 2001). These ligaments develop a capillary instability and break up into small droplets ($D_G < D_l$) located on the periphery of the jet. However, atomization induced by this process is not dominant. Beyond a few D_l, the shear instability is damped and the jet is disrupted by the growth of a capillary instability (λ'_R in figure 3*c*), producing droplets with diameters of the order of D_l on the injection axis. The mean λ'_R was found to be $\simeq 2D_l$, i.e. $\lambda'_R < \lambda_R$. The increase of the gaseous Weber number thus leads to a decrease of the capillary instability wavelength as a consequence of the increasing influence of the gas flow aerodynamics. The breakup length is also shorter for this regime, as can be seen in Appendix A.

The membrane regime is bounded by limits C and D in figure 3(*f*). The gasdynamics is strong enough to stretch the jet into an 'S' shape, about $4D_l$ to $8D_l$ long, as can be seen in figure 3(*d*). The gas impinges on the curved jet and creates a stagnation flow from which membranes are formed. The atomization of the membranes produces very small droplets, and the breakup of the peripheral rims leads to bigger droplets. Drop-size distributions measured for $Z = Z_D = 82.5$ mm, along the Y axis at several X positions, were thus found to be bi-modal. The main peak is located at $D_G = 700$ μm and the secondary one near $D_G = 100$ μm. The main mode comes from atomization of the rims, whereas the secondary peak is due to disintegration of the membranes. The breakup length is again shorter for this regime than for the shear breakup regime (see Appendix A).

The fibre-type regime occurs for $We \gtrsim 300$ and is bounded by limit D in figure 3(*f*). As this regime occurs for $Ma > 0.3$, compressibility effects may become non-negligible for the gas flow. Short and thin liquid fibres are created at the nozzle exit and are rapidly atomized by the air flow (figure 3*e*). The remaining liquid core, under the action of the gaseous jet turbulence, breaks into clusters and filaments along the injection axis (Lasheras & Hopfinger 2000). As the momentum flux ratio J increases, the breakup length and the size of the clusters decrease, and the number of clusters grows. The breakup length was found to decrease as J to the power $-1/2$ (see Appendix A). Bi-modal drop-size distributions were also obtained for the fibre-type regime. The main peak of the distribution is $D_G \simeq 60$ μm for all measurement locations, but at $X = 0$ a secondary peak appears for large droplets. This secondary peak is located around $D_G = 600$ μm for $We = 1193$ and shifts to lower values when We is increased. For the largest Weber number accessible with our experimental set-up, i.e. $We = 3314$, this peak reaches $D_G = 200$ μm. The secondary peak is induced by the formation of large liquid clusters and filaments, occurring mainly along the injection axis. Whatever the radial positions, the Sauter mean diameter D_{32} decreases in proportion with We^{-1} when the jet is in the fibre-type regime, as shown in figure 4. This is in agreement with correlations found in the literature (see for example Gomi 1985; Ingebo 1992; Hopfinger & Lasheras 1994; Vingert *et al.* 1995).

The spray angle θ was determined from series of 20–50 images. The minimum image of the image series is computed to determine all the possible locations of the droplets in the injection chamber. As can be seen in the work by Raynal (1997), the spray angle is determined from this minimum image and thus delimits the space in

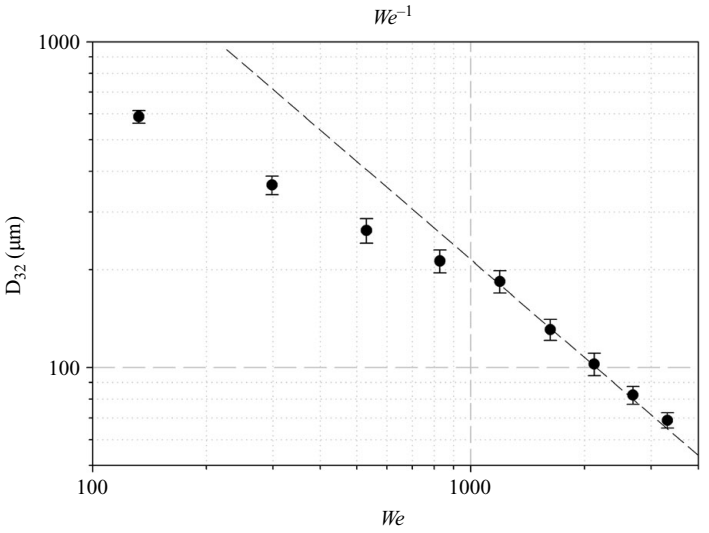

FIGURE 4. Sauter mean diameter as a function of We for $Re_l = 3536$ at relative downstream position $Z/D_g = 10.3$ and $X = 0$.

which all the spray is included, the apex being placed at the nozzle exit. The variation of θ is given in (3.1). Obviously, θ is null for the axisymmetric Rayleigh regime:

$$\theta = \begin{cases} 0 & \text{for axisymmetric Rayleigh regime,} \\ 40\log\left(\frac{We}{25}\right) \pm 7 & \text{for non-axisymmetric Rayleigh, shear and membrane regimes,} \\ 98 - 40\log\left(\frac{We}{25}\right) \pm 4 & \text{for fibre-type regime.} \end{cases} \tag{3.1}$$

For non-axisymmetric Rayleigh breakup, shear and membrane regimes, θ increases with We and reaches a maximum value around 45° in the membrane regime, in agreement with results of Raynal (1997). In the fibre-type regime, the spray angle decreases with a slope exactly opposite to the previous one. It is suggested that the decrease of the spray angle is related to the enhanced entrainment of the droplets or to the compressibility of the gas, since the fibre-type regime appears for $Ma > 0.3$.

3.2. *Acoustics without jets*

3.2.1. *Acoustic field*

The acoustic field was characterized by measuring the local pressure fluctuation amplitudes p' in the cavity. Figure 5 presents $p'(X)$ measured at $Y = 0$ and $Z = Z_D = 82.5$ mm for the excitation frequencies used in this work, $f_1 = 1000$ Hz and $f_2 = 1950$ Hz. For $f = f_1$, there is a pressure anti-node at $X = 0$ and two pressure nodes at $X = \pm L_c/4$. For $f = f_2$, there are three pressure anti-nodes in the cavity. In the volume defined by $-L_c/2 < X < L_c/2$, $0 < Z < 20D_l$ and $20D_l < Y < 20D_l$ the amplitude of the pressure fluctuations was almost constant (its variations are below 5 %) and no phase difference was detected in planes parallel to $(O, \vec{Y}\vec{Z})$. This volume covers the domain mainly occupied by the coaxial liquid core and the spray when the acoustics is turned off. Pressure at the pressure nodes is not quite null (see figure 5). This feature may be due to the integration of the measurement on the sensitive area of the sensor ($\simeq 5\,\text{mm}^2$), the dynamic range of the sensor and also the non-perfect reflection on the cavity walls. For $f_1 = 1000$ Hz, the harmonic modes of the cavity

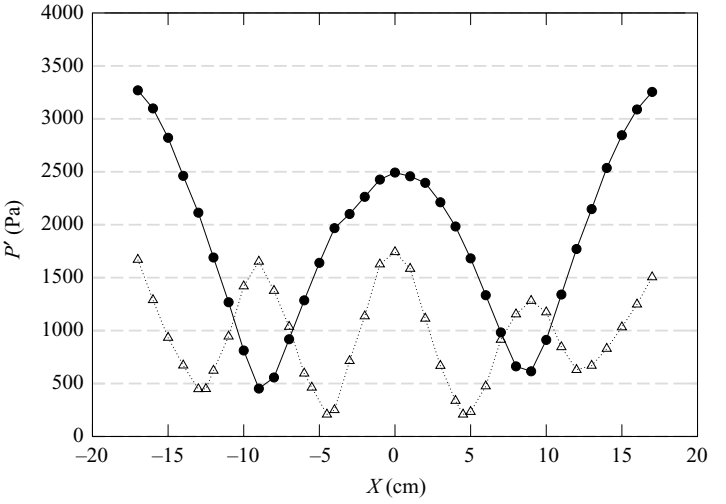

FIGURE 5. Acoustic pressure amplitude along the driver unit axis: ●, $f = 1000\,\text{Hz}$; △, $f = 1950\,\text{Hz}$.

($f = m \times f_1, m \geqslant 2$) were found to be negligible: the first harmonic, which is the most energetic one, has a power spectrum amplitude 100 times smaller than the main peak. Hence, the acoustic field can be interpreted as a planar standing wave in the $\overrightarrow{X}$ direction, corresponding to the second transverse mode of the cavity. Thus, pressure anti-nodes are velocity nodes and vice versa. For $f_1 = 1000\,\text{Hz}$, pressure and velocity acoustic fields in the cavity can be expressed by

$$P'(X, t) = P_{ac}\cos(kX)\cos(\omega t), \tag{3.2}$$

$$V'(X, t) = \frac{P_{ac}}{\rho_g c}\sin(kX)\sin(\omega t), \tag{3.3}$$

where $k = 2\pi/L_c$, $\omega = 2\pi c/L_c$ and P_{ac} is the maximum amplitude of the pressure fluctuations at the cavity centre.

The acoustic level in the cavity is referenced hereafter by P_{ac}. For $f = f_1$ the maximum value reached by P_{ac} was 3600 Pa, i.e. 3.6 % of the mean atmospheric pressure corresponding to a maximum SPL of 165 dB. Consequently, the maximum velocity fluctuation amplitude was estimated to be of the order of $8\,\text{m}\,\text{s}^{-1}$ at the pressure nodes. For $f = f_2$, the maximum pressure amplitude was 2150 Pa (i.e. 160 dB).

Three locations were chosen for the injector: the pressure node ($X = L_c/4$) and the velocity node ($X = 0$) for $f = f_1$ and the pressure node ($X = L_c/8$) for $f = f_2$. The amplitude and frequency of the pressure signal were controlled by an additional microphone positioned just under the roof, at the edge of the cavity.

The vibrations of the solid structure and of the injector, induced by the acoustic field, were measured and found to be very weak. The upstream quiescent cavity of the injector (see figure 5), characterized by a resonant frequency around 180 Hz was also found to be unperturbed by the pressure oscillations inside the cavity ($\delta p < 0.01 P_{ac}$).

3.2.2. *Nonlinear acoustics*

The particular behaviour observed for the liquid flow under the action of high acoustic levels led us to presume the action of nonlinear effects in the cavity. Acoustic streaming (i.e. non-zero mean flow) and radiation pressure (i.e. non-zero

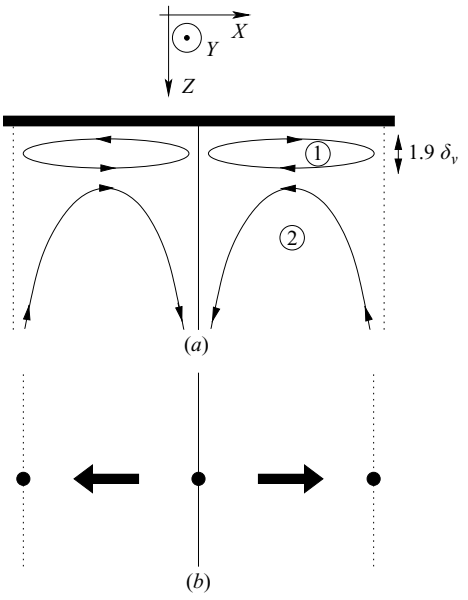

FIGURE 6. (*a*) Theoretical streamlines of the mean flow created by nonlinear acoustics streaming near a wall for $M \gg 1$ (①, Schlichting solution; ②, Rayleigh solution). (*b*) Radiation pressure force orientation between pressure node and pressure anti-node planes: ––, pressure node; —, pressure anti-node.

mean pressure) are such nonlinear effects. The flow motion induced by acoustic streaming depends on the value of the non-dimensional number M given in (3.4). This number compares the characteristic acoustic length $L_c/4$ to the oscillating viscous boundary layer thickness $\delta_v \sim \sqrt{\nu_g/\omega}$ that arises at the wall (Petit & Gondret 1992; Boluriaan & Morris 2003):

$$M = \frac{L_c}{4}\sqrt{\frac{\omega}{\nu_g}}. \tag{3.4}$$

For $M \gg 1$, a vortex of thickness $\simeq 1.9\ \delta_v$ (called the Schlichting solution) develops near the wall between every pressure anti-node and pressure node. The flow motion at the wall is directed towards the pressure node (see figure 6*a*). Beyond $1.9\ \delta_v$, a counterflow (called the Rayleigh solution) occupies the remaining space. For $M \ll 1$, the boundary layer flow fills the entire domain. For $f_1 = 1000\,\text{Hz}$, δ_v at the roof of our resonant cavity was about 50 μm, leading to $M \simeq 1000$. Thus, except inside the boundary layer, any acoustic streaming induced by the roof would be essentially dominated in the cavity by a stream moving from the pressure node towards the pressure anti-node, as shown in figure 6(*a*).

The acoustic radiation pressure p_{rad} is defined by the difference between the time-averaged potential and kinetic acoustic energies (Landau & Lifchitz 1989; Lee & Wang 1993):

$$p_{rad} = \frac{\langle p'^2 \rangle}{2\rho_g c^2} - \frac{\rho_g}{2}\langle \boldsymbol{u}'\boldsymbol{u}' \rangle + K \tag{3.5}$$

with K a constant generally equal to zero (the acoustic wave is damped in an infinite volume).

When an object is placed in the oscillating acoustic field, the local radiation constraint acting on the object surface is given by (3.6) where $\boldsymbol{n}$ is the unit normal

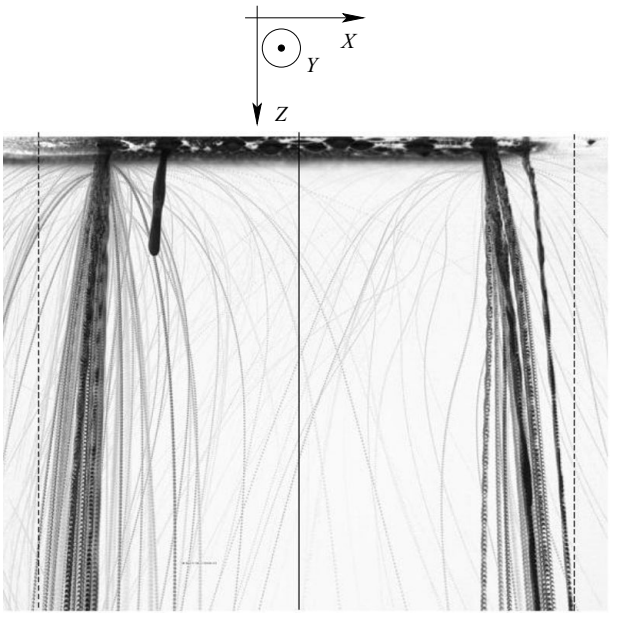

FIGURE 7. Experimental trajectories of droplets initially located under the roof for $P_{ac} = 3600\,\mathrm{Pa}$: ——, pressure node; —, pressure anti-node.

vector oriented towards the outside:

$$\boldsymbol{T}_{rad} = -p_{rad} \cdot \boldsymbol{n} - \rho_g \langle \boldsymbol{u}'(\boldsymbol{u}' \cdot \boldsymbol{n}) \rangle \tag{3.6}$$

For a perfect reflecting object, the velocity term vanishes (Mitome 1998). The resulting radiation force $\boldsymbol{F}_{rad}$ is expressed by

$$\boldsymbol{F}_{rad} = -\iint_{Sobj} p_{rad} \cdot \boldsymbol{n}\, \mathrm{d}S. \tag{3.7}$$

The movement induced by the radiation pressure on a liquid droplet has been studied by Hager & Benes (1991). The acoustic levitation of liquid drops has been investigated by Lee *et al.* (1991) and Yarin, Pfaffenlehner & Tropea (1998). Lierke (1996) showed that the force acting on a drop of diameter D_G may be expressed by

$$\frac{4F_{rad}}{\rho_g c^2 D_G^2} = -\pi \left(\frac{P_{ac}}{\rho_g c^2}\right)^2 \sin\left[\left(\frac{4\pi}{L_c}\right)\left(X - \frac{L_c}{4}\right)\right] f(\kappa), \tag{3.8}$$

where $f(\kappa)$ is a function of the non-dimensional parameter $\kappa = kR$ with k the acoustic wavenumber and R the radius of the sphere (see (5.3) for $\kappa \ll 1$). The radiation force is thus null at pressure nodes and pressure anti-nodes, is maximum in the middle of these two planes and is directed from the pressure anti-nodes to the pressure nodes, as shown in figure 6(*b*).

In order to determine the major nonlinear effect in our configuration, an experiment has been conducted without the liquid jet in the cavity. Water drops (a few millimetres in diameter) were placed under the cavity roof, and their motion was studied for $P_{ac} = 3600\,\mathrm{Pa}$ and $f = f_1$. The drop trajectories were obtained from images of a series recorded at 1000 images s^{-1} over $\sim$1 s. As drops appear in black over white in the image, the minimum-level image was computed to track them (see figure 7). Indeed, this calculation assigned to each pixel the minimum grey level it had in all the images of the series. Thus, the dark pixels in the minimum image keep track of the drops

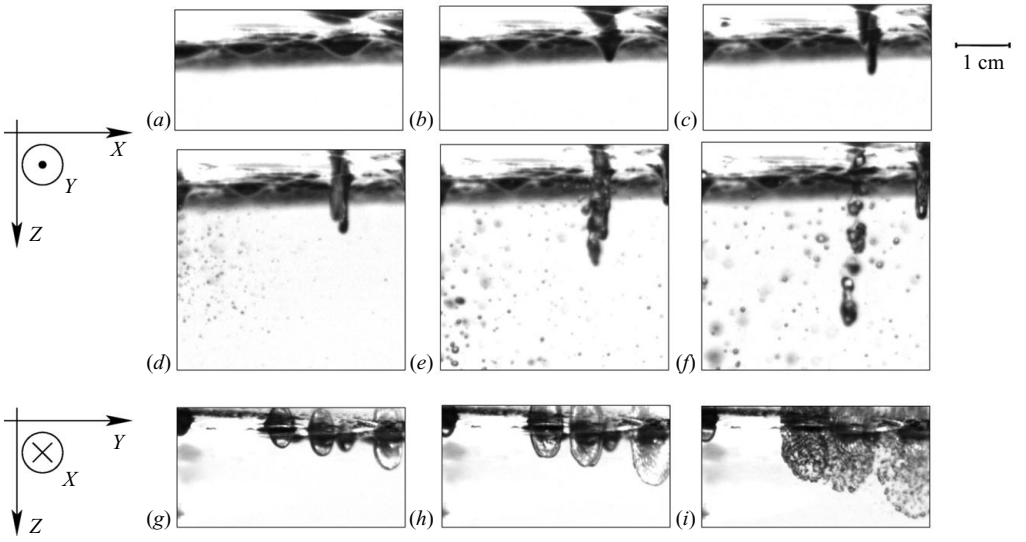

FIGURE 8. Magnified views of droplets placed under the roof under the action of the acoustic field ($P_{ac} = 3600$ Pa). (a–f) Front views. (g–i) Side views. The time interval between (a)–(f) or (g)–(i) is 15 ms. The pressure node is just at the left of the visualization field for (a)–(f), and the pressure anti-node is far from the right. The droplet flattening followed by an explosion into many little droplets is clearly shown in the side views.

passing over these pixels. As can be seen in figure 7, no trajectory starts from the pressure anti-node position, but two main trajectories start from positions near a pressure node plane. These trajectories are asymptotically converging towards the nearest pressure node plane. In addition to these two main trajectories, there are numerous parabolic-like trajectories that mostly converge towards the nearest main trajectory. The central pressure anti-node plane is reached by a few of the trajectories whose droplets have enough initial impulse, but they then pass over it and reach the next pressure node plane. The parabolic-like trajectories indicate a practically horizontal initial droplet velocity. Magnified views of drops placed under the roof are given in figure 8 to explain this particular motion. Indeed, drops placed near a pressure node plane are flattened. The liquid sheet so formed disrupts into a multitude of very small daughter droplets. These droplets are ejected perpendicular to the liquid sheet, i.e. to the vertical plane, leading to initial horizontal motions.

First, the comparison between the droplet trajectories observed in figure 7 and the expected nonlinear acoustic effects in figure 6 suggests that the prevailing nonlinear effect in our experiment is due to the pressure radiation. Indeed, the orientation of the force resulting from the radiation pressure effect (see figure 6b) agrees with the trajectories followed by the droplets, whereas acoustic streaming cannot explain the trajectories. Secondly, acoustic streaming cannot lead to the droplet deformation, while in contrast, the deformation has been clearly identified as resulting from the radiation pressure field (see Lee *et al.* 1991 and Anilkumar, Lee & Wang 1993 for ultrasonic waves).

King (1934) developed a theoretical model that gave an analytical representation of the action of the radiation pressure on a rigid sphere. The sphere of radius R interacts with the acoustic wave and modifies the incident pressure field leading to a locally non-null radiation pressure on the sphere surface. Using King's results, we

developed the expression of the local radiation pressure around the surface of the sphere for a stationary plane acoustic wave with $\kappa \ll 1$:

$$p_{rad}(\zeta) = \frac{P_{ac}^2}{4\rho_g c^2} g\left(\kappa, \frac{X_G}{R}, \zeta\right). \tag{3.9}$$

In (3.9), X_G is the position of the centre of the sphere and ζ the cosine between the outside normal vector $\boldsymbol{n}$ and the acoustic axis direction $\overrightarrow{X}$. The function $g(\kappa, X_G/R, \zeta)$ is detailed in Appendix B. At a pressure anti-node, the radiation pressure is almost constant all around the sphere and simply acts as a mean pressurizing environment. At a pressure node, the radiation pressure presents a strong variation with a minimum negative value in the direction perpendicular to the acoustic axis, resulting in a dominant suction effect, as illustrated in Appendix B. It agrees with our observation of drop flattening.

Finally, nonlinear acoustic effects induced by a non-uniform radiation pressure distribution can act locally on liquid elements (i) by deforming them when radiation pressure, p_{rad}, can exceed local surface tension and (ii) by moving them when the resulting radiation force, $\boldsymbol{F}_{rad}$, is not null. Thus, for the coaxial jet studied here, this could result (i) in the deformation of the liquid core in the same way as for the drops placed under the cavity roof, since the jet diameter is of same order of magnitude as the drop size ($\simeq$ a few millimetres), and (ii) in the deviation of the movement of liquid elements from the jet (in particular, spray droplets with the same size as the daughter droplets coming from the breakup of the roof drops) as soon as the resulting radiation force can counterbalance their inertia.

4. Injection at a pressure anti-node

4.1. *Gas flow behaviour*

In this section, the injector was positioned at the pressure anti-node ($X = 0$). The schlieren technique was used to visualize the structure of the gas coflow. Longitudinal modulations at the acoustic frequency arose when the pressure amplitude fluctuations in the resonant cavity were large enough compared to the mean dynamic pressure of the gas flow. Indeed, when the external adverse fluctuating pressure p' is able to decelerate or even stop the gas-flow over a fraction τ of the acoustic period T, the flow rate during the remaining time $(1-\tau)T$ is increased and leads to the formation of a vortex. For $P_{ac} = 3600$ Pa, the vortex emission phenomenon was observed for We up to 300, i.e. for $U_g < U_{g,lim} = 52\,\mathrm{m\,s^{-1}}$. The limit dynamic pressure expressed with $U_{g,lim}$, $p_{lim}^{dyn} = \rho_g U_{g,lim}^2$ matches the acoustic pressure ($p_{lim}^{dyn} \simeq P_{ac}$). So when $p^{dyn} > p_{lim}^{dyn}$, i.e. when $p^{dyn} > P_{ac}$, acoustics can no longer counterbalance the gas impulsion at the injection.

The gas also presented small transverse periodic movements. It moved along the X axis at the frequency of the acoustic field, successively outwards and inwards on both sides of the pressure anti-node plane. This lateral movement is suggested to contribute to the increase in the spray cone angle shown hereafter. The transverse gas velocity amplitude was estimated from time-resolved visualizations ($\sim 1\,\mathrm{m\,s^{-1}}$ for $P_{ac} = 3600$ Pa and $X = 10$ mm). It fits well the theoretical acoustic velocity given by (3.3).

4.2. *Jet regimes under acoustics at a pressure anti-node*

For a non-assisted flow ($We = 0$), no change in the atomization regime was observed, whatever the value of P_{ac}. Equally, all the jet regimes previously identified were

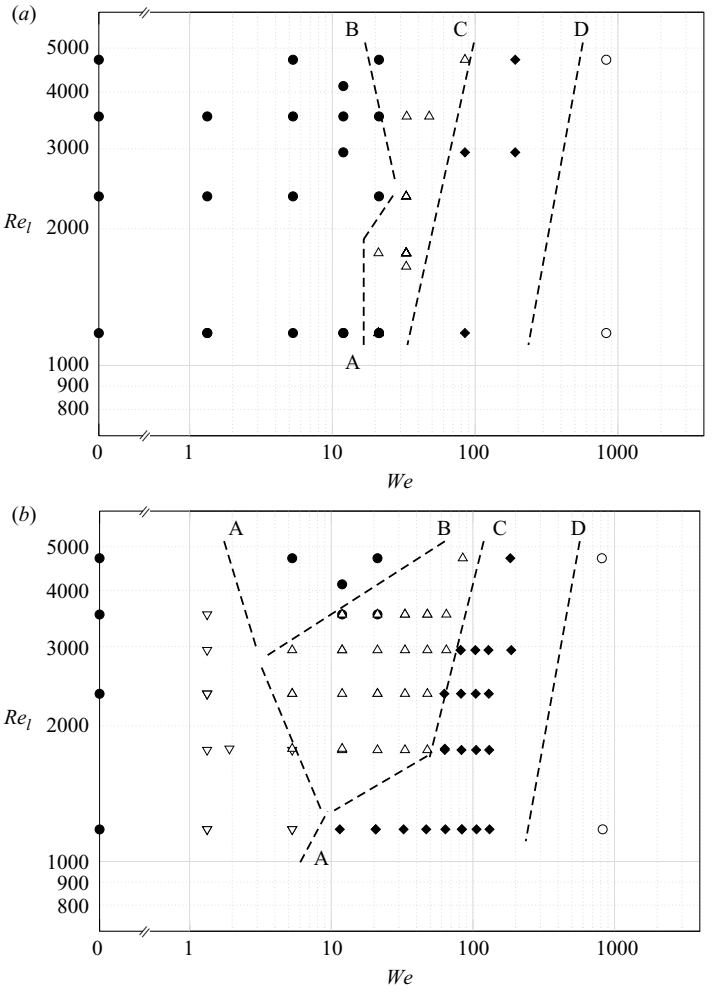

FIGURE 9. Diagram of the jet breakup regimes in the parameter space Re_l–We for the injector placed at $X = 0$: ●, axisymmetric Rayleigh; △, shear; ◆, membrane; ○, fibre; ▽, Rayleigh atomized. (*a*) $P_{ac} = 2160$ Pa, (*b*) $P_{ac} = 3600$ Pa.

unmodified ($We > 0$), whatever the flow conditions, as long as $P_{ac} < 720$ Pa. Moreover, schlieren visualizations confirmed that the gas modulation was not strong enough to induce any modification of the liquid–gas interface instabilities.

For $P_{ac} = 720$ Pa, the non-axisymmetric Rayleigh regime was replaced by the axisymmetric Rayleigh regime. Schlieren visualizations showed a symmetrization of the gas flow controlled by the vortex ejection. Limit B shown in figure 2(*b*) vanishes, but the other limits between the regimes are unmodified.

For $P_{ac} > 720$ Pa, the limits between regimes are shifted towards lower values of We as P_{ac} increases (see figures 9*a* and 9*b*), the largest shift occurring for the lowest value of We and Re_l. Schlieren visualizations showed that vortices induced by the gas modulation led to the development of an early shear instability which appears more easily for low We when P_{ac} is high. Thus, the pressure modulation is able to generate new surface instabilities when its amplitude is high enough compared to the mean dynamic pressure of the gas flow.

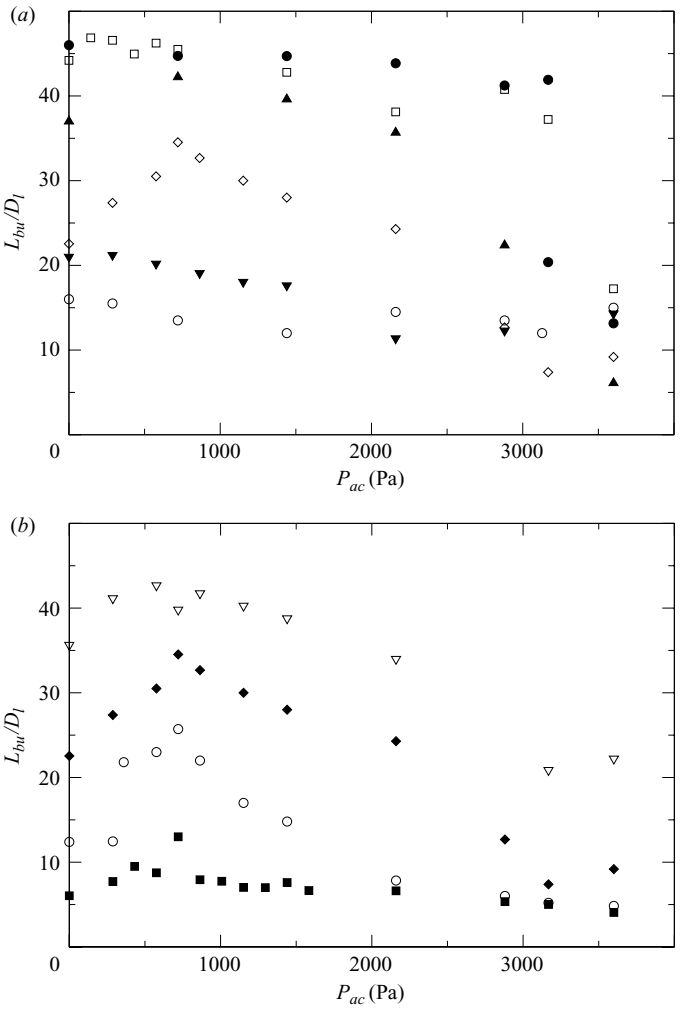

FIGURE 10. Evolution of the breakup length with P_{ac} for the injector placed at $X = 0$. (*a*) $Re_l = 3536$; ●, $We = 1.3$; □, $We = 5.3$; ▲, $We = 12$; ◇, $We = 22$; ▼, $We = 33$; ○, $We = 64$. (*b*) $We = 22$; ▽, $Re_l = 1179$; ◆, $Re_l = 2357$; ○, $Re_l = 3536$; ■, $Re_l = 4715$.

To conclude, the modifications in the jet regime limits result from the oscillating feature of the acoustic field on the longitudinal gas velocity and not from the mean radiation pressure. Indeed, the radiation pressure distribution has no effect on the liquid core near a pressure anti-node, even for non-assisted jets ($We = 0$), in agreement with previous experimental and theoretical results reported in § 3.2.2.

4.3. *Characteristic scales*

The breakup length

Although no change of the breakup length was observed for $We = 0$, i.e. $L_{bu} = L_{bu}^0$, acoustics modified L_{bu} as long as $0 < We \leqslant 64$, i.e. the lower limit of the shear breakup regime. This is illustrated in figure 10(*a*) for $Re = 3536$ and $1.3 \leqslant We \leqslant 64$. The general trend is a decrease of the breakup length as the acoustic level is increased, but it is less noticeable when We augments. Nevertheless, as We increases from 1.3 to 22, a stabilizing effect of acoustics is noticed (i.e. $L_{bu} > L_{bu}^0$) for $P_{ac} \leqslant P_{ac}^{stab}$

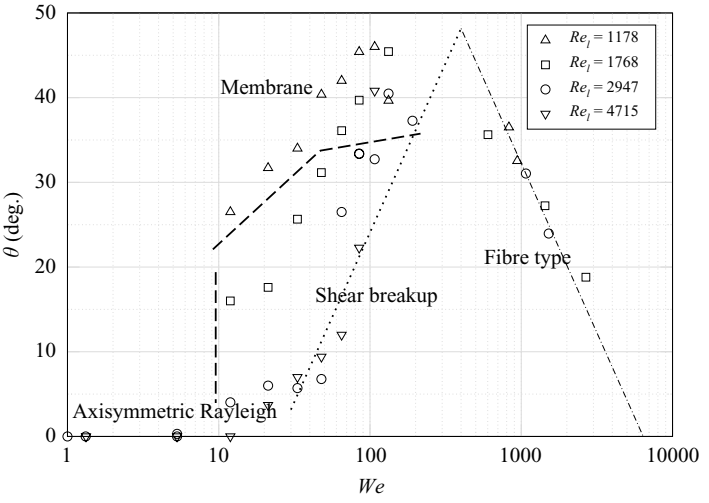

FIGURE 11. Spray angle versus We for the injector placed at $X = 0$ and $P_{ac} = 3600\,\text{Pa}$: —.—, $\theta = -40\log(We/25) + 48$; ···, $\theta = 40\log(We/25)$ ($P_{ac} = 0\,\text{Pa}$); —— limits between jet regimes.

(P_{ac}^{stab} ranging between 700 and 2000 Pa depending on We). The stabilization effect is maximum for $We = 22$ which marks the transition between the axisymmetric Rayleigh regime and the shear breakup regime. Figure 10(b) reports results for $We = 22$ and $1179 \leqslant Re_l \leqslant 4715$. Whatever the value of Re_l, L_{bu} augments with P_{ac} for $P_{ac} \leqslant P_{ac}^{stab}(We = 22) = 720\,\text{Pa}$ and then decreases. The increase of L_{bu} is consistent with the fact that the non-axisymmetric Rayleigh breakup regime is replaced by the Rayleigh axisymmetric regime for $P_{ac} = 720\,\text{Pa}$. For $P_{ac} > 720\,\text{Pa}$, the breakup length decreases, and for the largest P_{ac}, it reaches values much lower than those measured without acoustics, revealing an early atomization phenomenon.

Capillary and shear wavelengths

The wavelength λ_R was measured only up to $We = 33$. No significant difference could be found between experiments with or without acoustics, i.e. $\lambda_R \simeq 3D_l$ for the Rayleigh axisymmetric regime and $\lambda_R \simeq 2D_l$ for the shear regime.

The shear wavelength λ_C globally decreases with Re_g for all P_{ac}, as found without acoustics, but with a wider range of values ($2e < \lambda_C < 10e$).

Spray angle

The spray angle, θ, has been measured with the same method as that used without acoustics. Its variation with We is shown in figure 11 for $P_{ac} = 3600\,\text{Pa}$. In the same way as without acoustics, θ first increases up to a maximum value of about 45°. However, this maximum is obtained for $We \simeq 100$, instead of $We = 400$ for $P_{ac} = 0\,\text{Pa}$. This is consistent with the shift of the limits between the jet breakup regimes towards lower Weber numbers (see figure 9). The spray angle varies as $1/Re_l$, but θ increases more steeply for the highest value of Re_l. The spray expansion may be affected by the radiation pressure, since it tends to make droplets move towards velocity anti-nodes. When the jet is in the fibre-type regime, the same decrease as the one obtained without acoustics is observed. Indeed, the gas flow modulation induced by acoustics is actually negligible compared to its mean dynamic pressure and consequently has no effect on the spray angle.

Drop-size distributions

Drop-size distributions were measured for the same flow conditions and positions as without acoustics. For jets in the fibre-type regime as well as in the membrane regime, no drop-size modification really emerged whatever the acoustic pressure amplitudes and the measurement positions X.

4.4. *Summary*

The breakup of a liquid jet placed at a pressure anti-node was affected by acoustics only if it was assisted by the coaxial gas flow. When P_{ac} was high enough ($P_{ac} > \rho_g U_g^2$), the transverse wave imposed a longitudinal modulation on the gas stream, capable of modifying the strain at the liquid–gas interface. The adaptation of the air coflow to the pressure modulation in the cavity led periodically to the formation of a vortex at the injection exit, even in this configuration of a sharp-edged nozzle between the two fluids. A change in the breakup length was observed for $We < 64$, a limitation directly related to the highest acoustic levels P_{ac} (3600 Pa) accessible in our experiments. For $We \leqslant 22$ acoustics actually stabilized the jet for $P_{ac} \leqslant P_{ac}^{stab}$. The stabilization was consecutive to the gas flow symmetrization induced by the vortex. On the contrary, for the other conditions ($We \leqslant 22$ and $P_{ac} > P_{ac}^{stab}$; $22 < We < 64$ for all P_{ac}) the unsteady strain enhanced the development of interfacial perturbations produced by an early shear instability, leading to the diminishing of the breakup length and to the shift of the limits between the jet regimes towards lower Weber numbers. The spray cone angle increased under the action of acoustics. It is suggested that the action of the resulting radiation force tends to push the droplets away from the pressure anti-node towards the pressure nodes, which increases the dispersion of the drops.

5. Injection at a velocity anti-node

In this section, the injector was placed at the acoustic velocity anti-node $X = L_c/4$. Schlieren visualizations of the gas flow have shown that no periodic longitudinal modulation was generated by the acoustic field. Only one puff was ejected from the injector exit when acoustics was switched on, due to the fast adaptation of the gas flow to the new conditions imposed inside the cavity. However, the gas was still subject to a transverse periodic movement along the X axis at the acoustic frequency. This motion was in phase on both sides of the pressure node plane. The transverse gas velocity measurements agree with the theoretical acoustic velocity $U_{ac} = 8\,\mathrm{m\,s^{-1}}$ for $P_{ac} = 3600\,\mathrm{Pa}$ and $X = L_c/4 + 10\,\mathrm{mm}$.

5.1. *Flattening of the jet and sheet aspect*

5.1.1. *From round to flat jet*

For P_{ac} strictly lower than 2150 Pa, no modification of the flow was observed. Above this limit, the round jet was stretched along the $(\vec{Y}, \vec{Z})$ plane, i.e. along the velocity anti-node plane, for jets initially in Rayleigh axisymmetric and non-axisymmetric regimes, shear breakup and membrane regimes (see figure 12). The modification of the jet geometry and the atomization process induced are illustrated in figures 13 and 14 for a jet initially in the axisymmetric Rayleigh regime ($Re_l = 3536$, $We = 1.3$) and for $P_{ac} = 2448\,\mathrm{Pa}$. Images are taken from two sequences recorded at a frame rate of 3300 images $\mathrm{s^{-1}}$. At the start of the sheet formation (figures 13*a–c* and 14*a–c*), the jet is stretched along the $(\vec{Y}, \vec{Z})$ plane and flattened in the $\vec{X}$ direction. Simultaneously, a rim is formed at the sheet edges. This rim prevents measurement of the real thickness of the sheet from the front views.

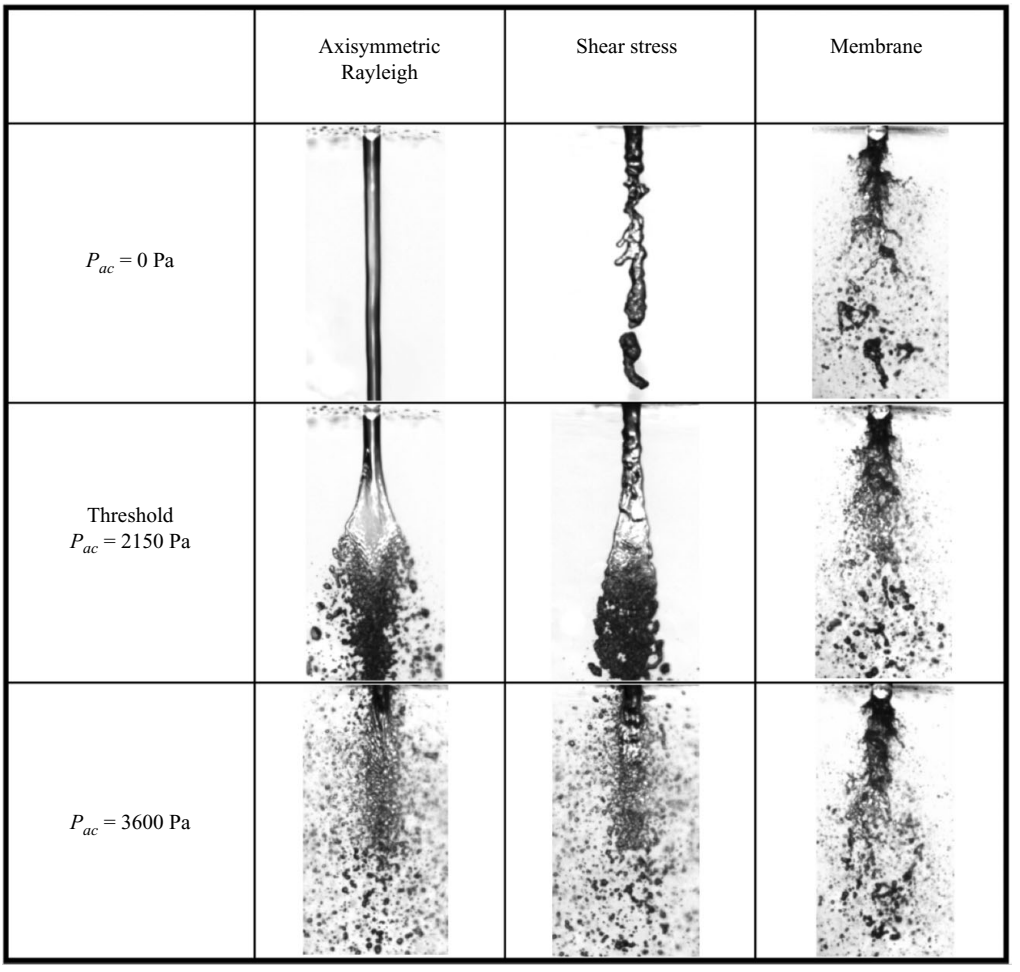

FIGURE 12. Jet behaviour for the injector placed at $X = L_c/4$ for several P_{ac} and initial jet regimes.

During the stretching of the jet, a net of perturbation waves appears, characterized by successive spatial crests and valleys leading to the ejection of droplets perpendicular to the sheet plane (see figure 14*e*). As the shape of the sheet boundary changes, the structure of this perturbation net evolves, depending on how the sheet edges are modified. In the last phase of the sheet formation (figures 13*e–f* and 14*e–f*), membranes near the bottom edges of the sheet disintegrate into droplets and rims are atomized into quite large drops whose trajectories are ballistic. The central part of the sheet breaks into large clusters of liquid, trapped in the sheet plane.

So, acoustics does flatten jets whatever the regimes, except for the fibre regime, whereas such a flattening has been reported in the literature only for non-assisted cylindrical liquid jets, as mentioned in § 1 (see for example Buffum & Williams 1967; Hoover *et al.* 1991; Oschwald *et al.* 2006; Carpentier *et al.* 2009). Unlike what occurred at the pressure anti-node, the oscillating gasdynamics is not the dominant mechanism. The flattening of the jet results from the radiation pressure effects described in § 3.2. Indeed, the liquid jet is not rigid; so it may be deformed into a sheet by the mean radiation pressure gradient distribution that develops around the jet circumference as

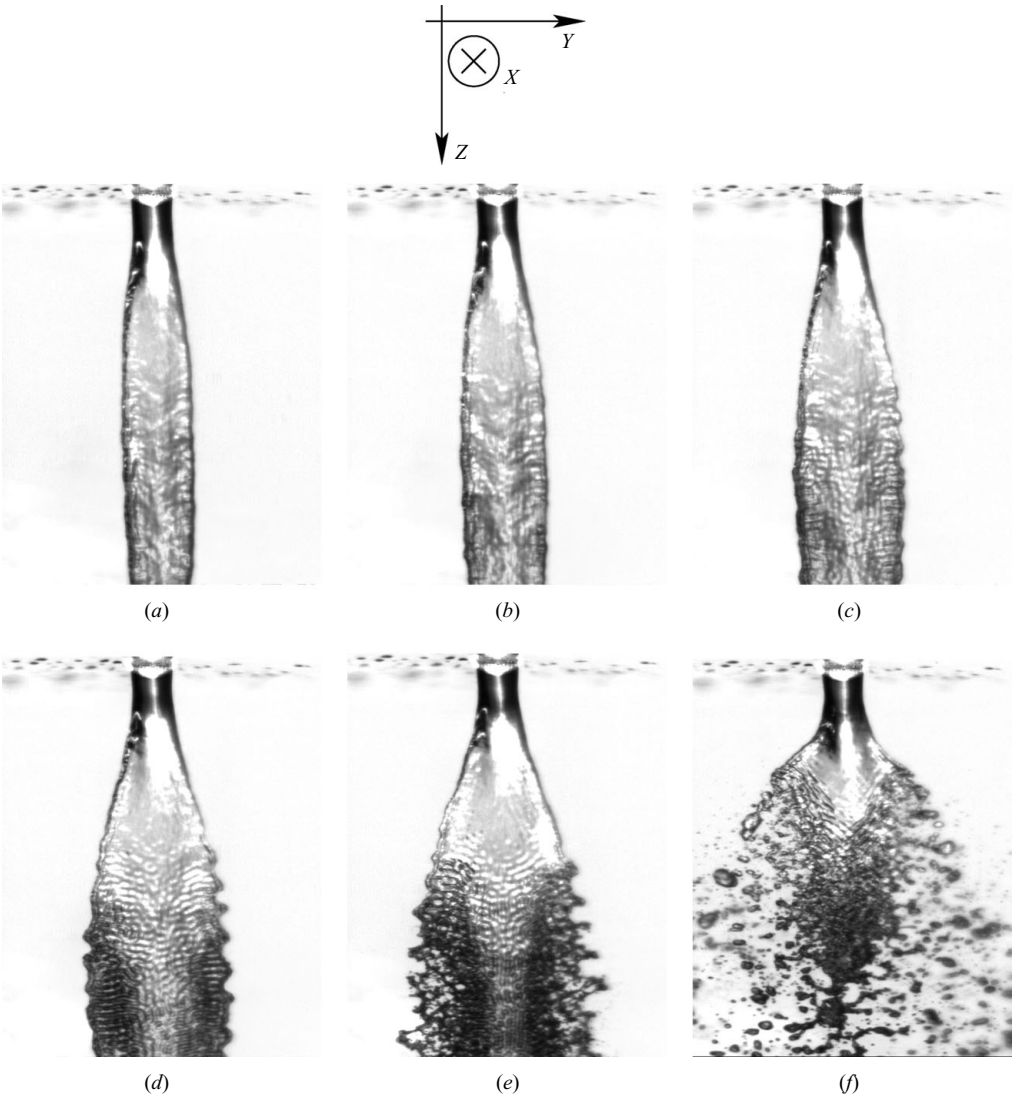

FIGURE 13. Time-resolved side views at $We = 1.2$, $Re_l = 3536$, $P_{ac} = 2448$ Pa. (*a–e*) Transformation of the jet into a sheet; time interval between two successive frames is 2.8 ms. (*f*) Sheet in its steady state.

soon as the surface tension can no longer sustain the action of this spatial radiation pressure distribution. This is detailed in the next section.

In addition, progressive longitudinal waves can be observed simultaneous to the sheet formation for jets that are initially only in the axisymmetric Rayleigh regime. These waves, characterized by a wavelength λ_p (about 1.5 mm, whatever Re_l and We) and a frequency equal to the frequency of the acoustic field, propagate from the edge towards the jet axis with a convection velocity about $1.5\,\mathrm{m\,s^{-1}}$ whatever P_{ac}. Theoretical convection velocities of capillary waves propagating on the surface of a liquid either of infinite depth (V_∞) or of depth $h = 2$ mm ($\simeq$ the thickness of the rim) for the varicose mode (V_v) and the sinuous mode (V_s) (Taylor 1959) are $V_\infty = 0.54\,\mathrm{m\,s^{-1}}$, $V_v = 1.3\,\mathrm{m\,s^{-1}}$ and $V_s = 7\,\mathrm{m\,s^{-1}}$. Thus, the convection velocity V_p matches

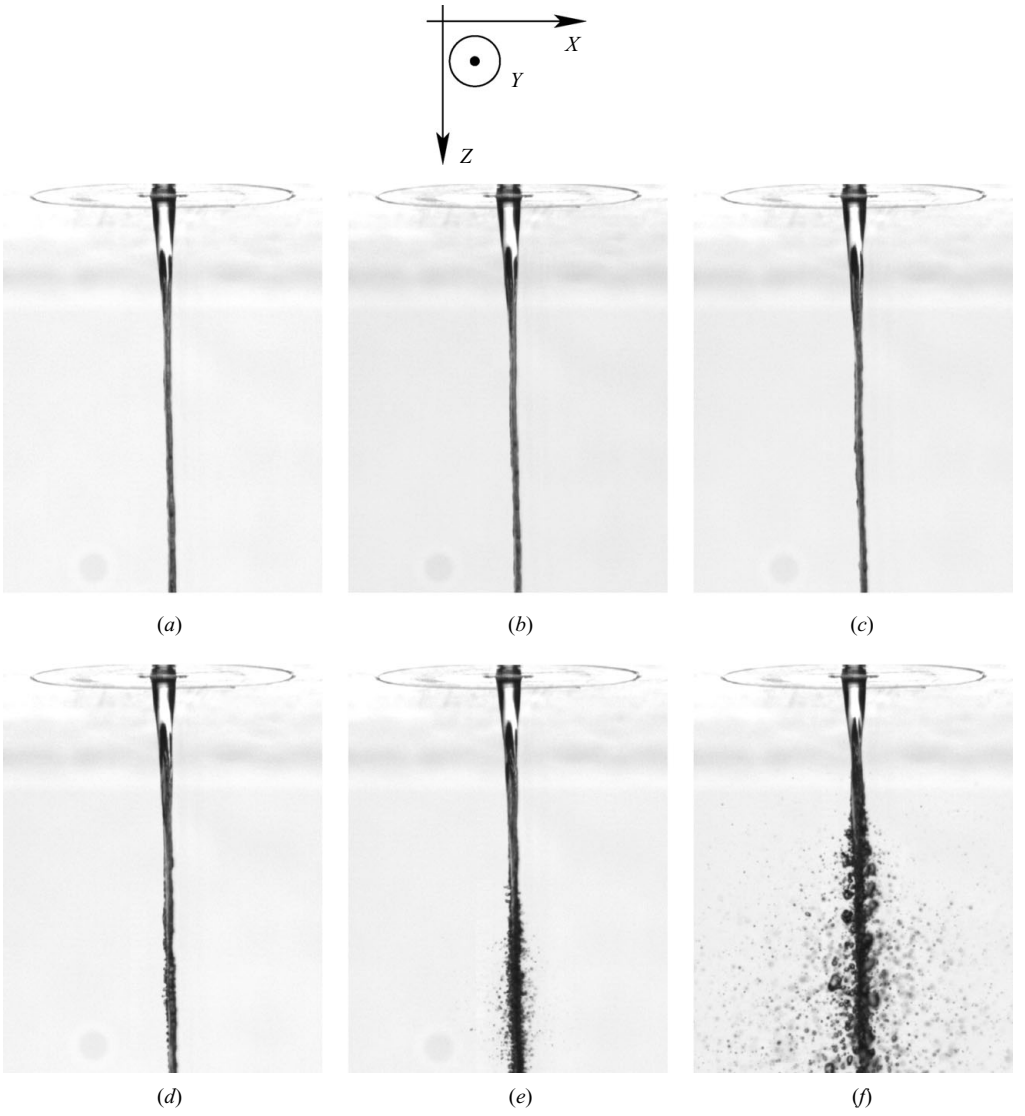

FIGURE 14. Time-resolved front views at $We = 1.2$, $Re_l = 3536$, $P_{ac} = 2448$ Pa. (a–e) Transformation of the jet into a sheet; time interval between two successive frames is 2.8 ms. (f) Sheet in its steady state.

the theoretical convection velocity of capillary waves propagating on the surface of a liquid film in the varicose mode. For jets initially in shear or membrane regimes, the sheet edges are so disturbed by the gasdynamics that such waves cannot be observed (see figure 12).

5.1.2. *Radiation Bond number criterion*

The deformation took place suddenly for all the regimes except the fibre regime when the acoustic pressure exceeded a given threshold, P_{ac}^{th}. Using (3.9) derived from the model of King (1934), the maximum local tensile stress $\boldsymbol{T}_{rad}^{max} = -\, p_{rad}^{min}\boldsymbol{n}$ at the interface of the jet placed at the velocity anti-node was estimated, even though the spherical geometry used for the calculation does not correspond to the

f (Hz)	1000	1950	1000
σ (N m^{-1})	0.072	0.072	0.052
P_{ac}^{th} (Pa)	2150	1830	1850
Bo_{ac}^{th}	1.2 ± 0.1	0.9 ± 0.1	1.3 ± 0.1
Bo_{rad}^{th}	0.28 ± 0.05	0.29 ± 0.05	0.28 ± 0.05

TABLE 1. Threshold values of P_{ac}, Bo_{ac} and Bo_{rad} at which the jet flattens (injector placed at $X = L_c/4$).

cylindrical configuration of the jet. At the threshold value (i.e. $P_{ac}^{th} = 2150$ Pa for water and $f = 1000$ Hz), we found a maximum suction effect, $p_{rad}^{min} = -17.3$ Pa acting in the direction perpendicular to the acoustic axis. This value is of the order of the pressure due to surface tension, i.e. $2\sigma/D_l = 24$ Pa. So, the radiation pressure is able to counterbalance the surface tension effect to induce the flattening of the round jet into a sheet.

In order to determine a criterion for the acoustic pressure threshold above which the jet flattening occurs, additional experiments were performed. A second acoustic frequency ($f_2 = 1950$ Hz) and another fluid (water–acetone mixture, 90 %/10 % in mass respectively) were tested. The mixture was chosen for its density, similar to that of water ($(\rho_l - \rho_{mix})/\rho_l \sim 0.02$), and its lower surface tension (0.052 N m^{-1} instead of 0.072 N m^{-1}).

The acoustic pressure threshold P_{ac}^{th}, reported in table 1, increases when σ increases and decreases when f increases. It can be noted that the usual acoustic Bond number $Bo_{ac} = (D_l P_{ac}^2)/(2\sigma\rho_g c^2)$ introduced in the studies on acoustically levitated droplets (Lee *et al.* 1991; Anilkumar *et al.* 1993) cannot be used to express this acoustic threshold, since the threshold depends on f whereas the usual acoustic Bond number does not. A modified Bond number based on the radiation pressure is thus proposed here to take into account the variation with f. This is supported by King's calculation for which the acoustic force is proportional not only to P_{ac}^2 but also to κ^m, with $m = 1$ in the case of the spherical geometry. Thus we defined a radiation Bond number Bo_{rad} by

$$Bo_{rad} = \frac{D_l P_{ac}^2 \kappa^m}{2\sigma\rho_g c^2}. \tag{5.1}$$

It was found that $Bo_{rad}^{th} = 0.28 \pm 0.05$ for $f = 1000$ Hz and $Bo_{rad}^{th} = 0.29 \pm 0.05$ for $f = 1950$ Hz, with $m = 0.5$ (see table 1). The value of m, different from the one found by King, can be explained by the different geometries, cylindrical in our case and spherical in the case of King's calculation. The value of the radiation Bond number threshold, Bo_{rad}^{th}, is also confirmed by experiments, originally carried out to quantify the dynamics of the jet deformation from its round to its flat aspect, as presented hereafter in § 5.2.

Moreover, this criterion is in accordance with the experiment of Buffum & Williams (1967) for which the maximum radiation Bond number is estimated to be around 0.01 at which no transformation of the jet into a sheet was reported. Carpentier *et al.* (2009) gave indicative critical Weber number values corresponding to the occurrence of liquid sheet atomization from a non-assisted jet. These values, converted to the present radiation Bond number, lead to rough threshold values (0.15–0.38) in agreement with Bo_{rad}^{th}. Hoover *et al.* (1991) observed the flattening of the jet as soon as a specific acoustic amplitude was reached. To apply our criterion to their results,

it is necessary to correctly evaluate this acoustic amplitude. Indeed, the field present in their cylindrical test chamber results from the eigenmode $1T - 3L$ for which the acoustic pressure amplitude given by the authors is not the maximal amplitude imposed on the jet. From their configuration, we estimated the pressure amplitude threshold P_{ac}^{th} to be around 1100 Pa, leading to a threshold $Bo_{rad}^{th} \simeq 0.11$. According to this rough estimation, the result can be considered consistent with our criterion.

Davis & Chehroudi (2006) did not observe the flattening phenomenon with their coaxial configuration. Indeed, the root mean square (r.m.s.) acoustic pressure amplitude ranged from 0.3 % when the chamber pressure was maximum (i.e. at a near-critical pressure $\simeq 5$ MPa) to 2 % when the chamber pressure was mimimum (i.e. at a subcritical pressure $\simeq 1.5$ MPa) (see Davis 2006). But the acoustic field was not a pure standing wave arising from a sinusoidal source. At the minimum pressure location of their field, large 'residual' acoustic pressure amplitudes persisted (pressure r.m.s. $\simeq 1$–3×10^4 Pa compared to the value lower than 350 Pa measured here) and transverse acoustic velocity amplitudes were very small (velocity r.m.s. $\simeq 1\,\mathrm{m\,s^{-1}}$ compared to $7\,\mathrm{m\,s^{-1}}$ here). Thus, the minimum pressure is far from a strict pressure node. Consequently, in the subcritical case, fluctuations of the incident wave could not induce the appropriate scattered acoustic field at the liquid–gas interface that would lead to a radiation pressure distribution (and particularly powerful suction; see King 1934 and Yarin *et al.* 1998) capable of counterbalancing surface tension effects. Moreover, in the near-critical case, the existence of a non-well-defined interface disturbed the formation of the scattered field and consequently the appropriate radiation distribution. However, as proposed by the authors, a vortex shedding mechanism could be triggered by the thick injector lip configuration. So, the lip of the inner tube might interact with the acoustic wave to cause the large-scale motions of the liquid core.

5.2. *Characteristic scales measured on the flattened jet*

Four new atomization processes were identified from flattened jets (see figures 13*f* and 14*f*): atomization of the net by the ejection of droplets perpendicular to the sheet plane, breakup of the rim into droplets whose size is of the order of the rim radius, disintegration of thin membranes located at the sheet periphery and shedding of large clusters of liquid along the injection axis. These processes have replaced those observed without acoustics for jets initially in the axisymmetric, non-axisymmetric or shear breakup regimes. For jets initially in the membrane regime, membranes are still created and atomized under the influence of aerodynamic effects.

New scales have been identified in the images of the flattened jet as shown in figure 15. The intact length along which the liquid jet is almost cylindrical is denoted by L_i. The angle of the upper side of the sheet θ_s is measured from the modified side views of the jet; L_b and λ_b are lengths relative to the rim of the sheet and λ_n to the net occurring on the sheet itself.

Intact length L_i and sheet angle θ_s

For given Re_l and Re_g, the intact length, L_i, is a function of the difference $P_{ac} - P_{ac}^{th}$ only and does not depend on the nature of the liquid. Hence, the surface tension influences L_i only through the acoustic threshold P_{ac}^{th} and not according to how L_i evolves with P_{ac}. The variation of L_i typically relies on the initial jet regime (i.e. without acoustics). For jets initially in the axisymmetric and non-axisymmetric Rayleigh regimes, L_i is driven by the couple (P_{ac}, Re_l): it increases either when P_{ac} decreases or when Re_l increases. In the shear breakup regime, increasing Re_l or Re_g results in an increase of L_i. But, the influence of Re_g overlaps that of Re_l

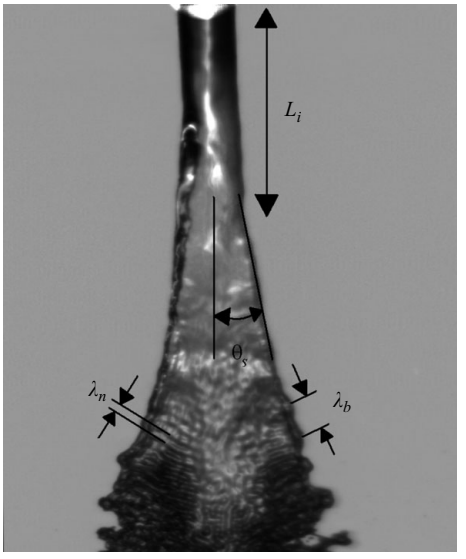

FIGURE 15. Characteristic scales of the sheet: λ_n, wavelength of the net; λ_b, wavelength of the rim instability; L_i, intact length of the jet; θ_s, sheet angle.

as We becomes higher; i.e. aerodynamic effects become predominant. Raising P_{ac} induces a decrease of L_i as was observed with the two previous regimes. For jets initially in the membrane regime, L_i increases with Re_g but is insensitive to Re_l, confirming that aerodynamic effects completely supersede hydrodynamic effects. No remarkable modification of L_i was noticed when P_{ac} was increased ($P_{ac} > P_{ac}^{th}$). The action of acoustics appears to be efficient when the gaseous mean dynamic pressure does not locally prevent the development of the radiation pressure field which creates new boundary conditions around the liquid jet. The mean vertical gas velocity U_{gLi} measured at $Z = L_i$ with a Pitot probe, but without the water jet and without acoustics, was found to be always of the order of 30–40 m s^{-1}. This value appears as a local critical gas velocity beyond which nonlinear acoustic effects (limited here by $P_{ac} = 3600$ Pa) cannot counterbalance aerodynamic effects. This could also explain the absence of sheet formation for jets in the fibre-type regime. In fact, for such a jet, the gas velocities are always greater than 50 m s^{-1} for $Z < L_{bu}^0$ ($L_{bu}^0/D_l \leqslant 15$), thus greater than the critical velocity mentioned above.

As long as the jet still presents a liquid core, flattening at the velocity anti-node is possible if acoustics can counterbalance (i) the surface tension, by creating the right radiation pressure distribution around the liquid jet, and (ii) the local gasdynamics, through its momentum flux $\rho_g U_g^2$. The amplitude limit $P_{ac} = 2150$ Pa above which flattening is observed here satisfies (i) and leads to a maximum gas velocity of 40 m s^{-1} to fulfil (ii). In practice, such aerodynamic conditions are fulfilled around the liquid core at the distance $Z = L_i$ for all the jet regimes, except the fibre regime. Indeed, for the fibre regime, gas velocities always remain greater than 50 m s^{-1} along the liquid core length L_{bu}. To satisfy (ii), it would be necessary to exceed $P_{ac} = 3600$ Pa, which is not accessible here. So, the criterion $Bo_{rad} = Bo_{rad}^{th}$, previously introduced, is efficient to describe the jet flattening observed here. But this 'acoustic' criterion might possibly be adapted to include the fibre regime configuration, by taking into account the local gas velocity related to L_i. Indeed, L_i is correlated to L_{bu}/D_l which evolves like $J^{-0.5}$.

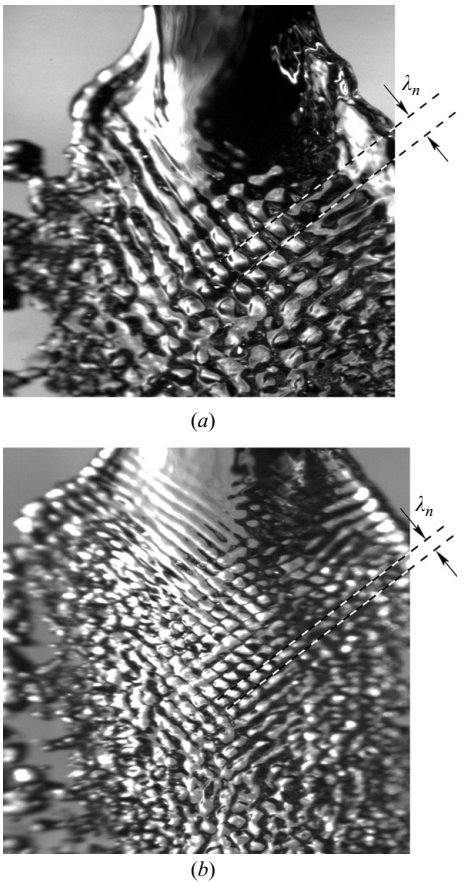

FIGURE 16. Aspect of the net instability at the surface of the sheet for $We = 1.3$, $Re_l = 3536$, $X = L_c/4$ and $Bo_{rad} > Bo_{rad}^{th}$. (*a*) $f = f_1 = 1000$ Hz. (*b*) $f = f_2 = 1950$ Hz.

The sheet angle θ_s (see figure 15) is found to be linked to the intact length L_i; θ_s decreases when L_i increases as $\theta_s = 100 - 1.25L_i$ (L_i in mm and θ_s in degrees). For the particular case in which L_i is null, θ_s is undefined.

Rim characteristics L_b and λ_b

The sheet is bounded by a thick rim formed in the same way as for the usual liquid sheet systems (see for example Brenn *et al.* 2005). The thickness L_b of the rim remains equal to 2 mm for all the acoustic and flow conditions. The rim is deformed by an instability of wavelength λ_b that remains almost constant and equal to 5 ± 1 mm.

Net characteristics λ_n

The wavelength λ_n characterizes the net of the instability which develops on the liquid sheet. This net is created by waves attached to the edges (the rims) of the sheet; λ_n remains constant with P_{ac}, U_l and U_g but is proportional to $1/f$ and σ (see figure 16 and table 2). The sheet located at a velocity anti-node is submitted to practically the highest fluctuating accelerations in the chamber, the action of which is perpendicular to the sheet. For $P_{ac} = P_{ac}^{th} = 2150$ Pa, the amplitude of the acceleration is about 3×10^4 m s^{-2} (i.e. 3×10^3 g). All these features are characteristic of the Faraday instability developing on liquid films in the absence of a mean flow (Faraday

f (Hz)	1000	1950	1000
σ (N m^{-1})	0.072	0.072	0.052
λ_n (mm)	1.4 $\pm$ 0.2	0.8 $\pm$ 0.1	1.1 $\pm$ 0.1
λ_f (mm)	1.21	0.78	1.09

TABLE 2. Wavelength of a net induced by a Faraday instability. Comparison between the experimental data λ_n and the theoretical values λ_f from Lang's formula (5.2).

1831) or in its presence (Woods & Lin 1995). To confirm the nature of the instability, λ_n is compared to the wavelength λ_f of the Faraday instability expressed by Lang (1962):

$$\lambda_f = \left(\frac{8\sigma\pi}{\rho_l f^2}\right)^{1/3}. \tag{5.2}$$

The theoretical λ_f calculated with (5.2) agrees well with the present data as seen in table 2. The net can present local structural defaults that produce a partial disorganization of the net liable to influence the sheet atomization. These defaults may come from the net itself which holds intrinsic instabilities as shown by Cabeza, Gibiat & Negreira (2003) from experiments on Faraday instabilities.

Dynamics of the jet deformation

Under the action of the acoustics, the jet is first flattened as a liquid sheet, and then the sheet so formed disintegrates into droplets. Here we focus our attention on the progressive modification of the shape of the liquid jet, as long as it remains continuous, i.e. before breakup occurs. The time from which the jet begins to flatten t_{ini} is essentially independent of fluid parameters Re_l and We but decreases with P_{ac}, as shown in figure 17(a). The acoustic field is still not stationary in the cavity at $t = t_{ini}$ (see figure 17b) to which correspond the transient acoustic pressure amplitude P_{ac}^{ini} and the associated radiation Bond number Bo_{rad}^{ini} given by (5.1). Figure 17(a) shows that $Bo_{rad}^{ini} \simeq 0.28$ for all the flow and acoustic conditions. Thus, it is verified that the radiation Bond number, Bo_{rad}^{ini}, at which flattening begins to transform the jet into a sheet when the acoustic amplitude rises from 0 to P_{ac}, has the same value as that of the radiation Bond number threshold, Bo_{rad}^{th}. This result confirms the threshold criterion defined previously for all the regimes (except the fibre regime), which marks the appearance of the liquid sheet (see § 5.1). It must be noted that the decreasing accuracy in the determination of Bo_{rad}^{ini} when P_{ac} increases is a consequence of the way the acoustic field is imposed in the cavity. Indeed, the setting-up time of the acoustic field is constant (60 ms); so the slope of the acoustic pressure envelope increases sharply with P_{ac}.

The dynamics of the sheet formation is qualified through the variation of Δ_s, the sheet width defined as the difference between the two extreme positions in the continuous liquid phase along the Y direction. Thus, measurements were carried out from time-resolved views only for $We \leqslant 33$. The evolution of Δ_s is plotted in figure 18 for $Re_l = 3536$, $We = 12$ and different acoustic levels. The width of the sheet increases exponentially with time and all the more rapidly as the acoustic level is high. For the last time ($t = t^{end}$) at which the measurement was possible, the sheet width is found to be around 32 $\pm$ 3 mm for all the experimental conditions (P_{ac}, We, Re_l). This corresponds to the sheet width for which the local thickness of the membranes became critical, i.e. above which the membranes disintegrated.

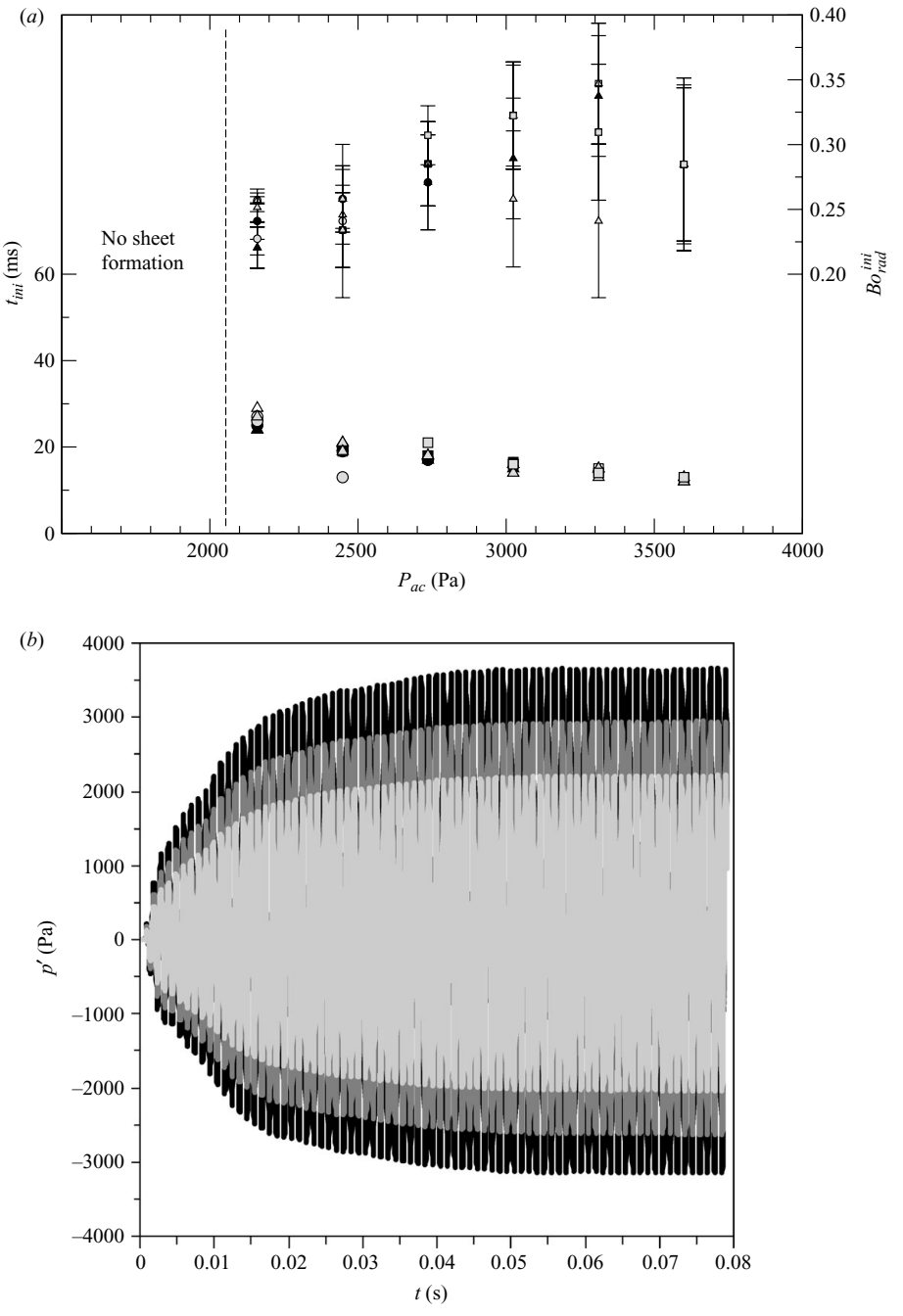

FIGURE 17. (*a*) Evolution of t_{ini} and Bo_{rad}^{ini} with P_{ac}: grey symbols, $We = 33$; black symbols, $We = 12$; empty symbols, $We = 0$; ●, ●, ○, $Re_l = 2947$; ▲, ▲, △, $Re_l = 3536$; ■, ■, □, $Re_l = 4715$. (*b*) Transitional pressure signal in the cavity for $P_{ac} = 3600$ Pa (■), $P_{ac} = 2736$ Pa (■), $P_{ac} = 2448$ Pa (□).

The expansion velocity of the sheet is determined from the mean displacement of the sheet edges over $\tau = 1$ ms: $V_{exp}(t) = (\Delta_s(t) - \Delta_s(t-\tau))/\tau$. For $t > t_{ini}$, V_{exp} grows exponentially with time for all the flow and acoustic conditions, consecutive to the

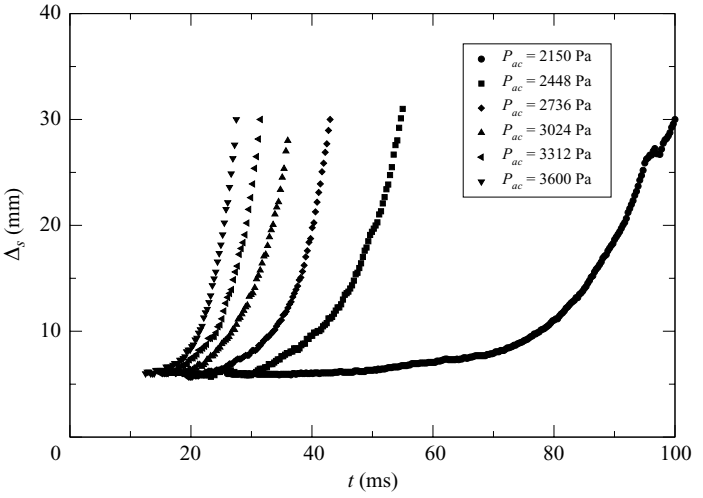

FIGURE 18. Evolution of Δ_s as a function of time for $Re_l = 3536$ and $We = 12$.

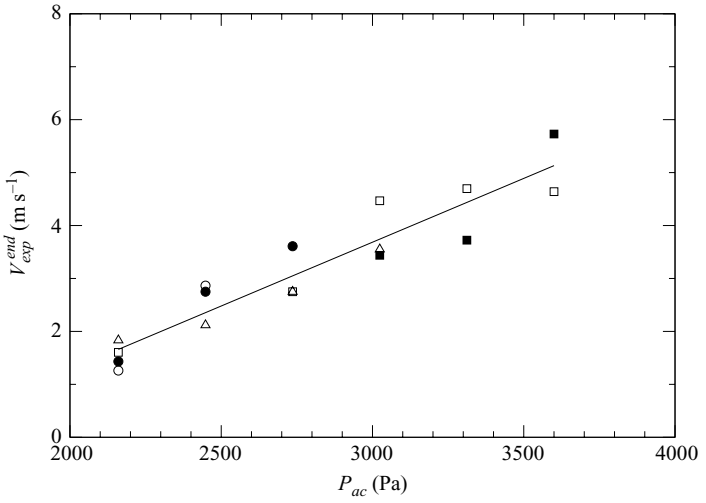

FIGURE 19. Evolution of V_{exp}^{end} with P_{ac}: black symbols, $We = 12$; empty symbols, $We = 0$; ●, ○, $Re_l = 2947$; ▲, △, $Re_l = 3536$; ■, □, $Re_l = 4715$; —-, regression $= 0.0024 P_{ac} - 3.5$.

exponential evolution of the sheet width Δ_s. The velocity estimated at $t = t^{end}$, i.e. V_{exp}^{end}, is plotted in figure 19 as a function of P_{ac} for all the flow conditions; V_{exp}^{end} is found to increase linearly as a function of P_{ac}.

The breakup length L_{bu}

The breakup length L_{bu} is still defined as the vertical length between the injector exit plane and the farthest downstream position belonging to the intact jet core; L_{bu} is greatly reduced under the action of acoustics. Figure 20 shows that L_{bu} always remains lower than L_{bu}^0, the breakup length without acoustics. In fact, $L_{bu} \leqslant 0.5 L_{bu}^0$ for $P_{ac} = 3600$ Pa. The increase in Re_l or the decrease in We results in an increase in L_{bu}, indicating that even in the presence of acoustics, the liquid dynamics and gasdynamics still act on the liquid behaviour. For $We > 60$, L_{bu} tends, from below, up to the values

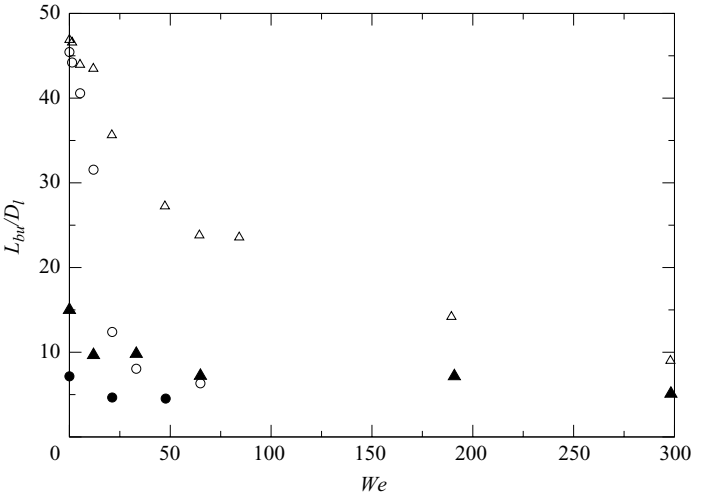

FIGURE 20. Reduced breakup length as a function of We for the injector placed at $X = L_c/4$ and $Z/D_g = 10.3$. ○, $Re_l = 2357$, $P_{ac} = 0$; ●, $Re_l = 2357$, $P_{ac} = 3600$ Pa; △, $Re_l = 4715$, $P_{ac} = 0$; ▲, $Re_l = 4715$, $P_{ac} = 3600$ Pa.

obtained without acoustics in the fibre-type regime ($We >$ 300–500). Transformation of the cylindrical jet into a sheet globally promotes atomization.

Drop-size distributions

Drop-size distributions were measured at the position $X = L_c/4 + 30$ mm (30 mm $\sim L_c/10$) on the acoustic axis ($Z = Z_D = 82.5$ mm, $Y = 0$ mm) for jets initially in the axisymmetric Rayleigh regime ($We < 22$). Droplets created by the pitching of crests due to the Faraday net and produced by the disintegration of the sheet membranes are ejected perpendicular to the sheet plane. The mean diameter D_{30} is measured in the range 240 μm $< D_{30} <$ 720 μm. Using the wavelength characterizing the instability net on the liquid sheet, this leads to $0.2\lambda_n < D_{30} < 0.6\lambda_n$. This is in agreement with the results of Sindayihebura, Cousin & Dumouchel (1997) for ultrasonic atomizers generating droplets from the Faraday instability mechanism. It is also found that drop-size distributions are quite similar, while light transmission decreases when P_{ac} increases. Thus, a rise in P_{ac} leads to an increase in the liquid volume atomized without changing the atomization processes.

5.3. *Droplet trajectories modified under the radiation pressure effect*

Particular droplet trajectories were observed from time-resolved visualizations. Several droplets ejected perpendicular to the liquid sheet went back towards the velocity anti-node. Figure 21 shows the curved trajectory of such a droplet characterized by a diameter $D_G = 400$ μm and an ejection transverse velocity $U_p^0 \simeq 0.64\,\mathrm{m\,s^{-1}}$ ($\pm 0.05\,\mathrm{m\,s^{-1}}$). The movement back to the velocity anti-node plane is interpreted as being caused by the action of the resulting radiation force $\boldsymbol{F}_{rad}$, expressed by (3.8), where $f(\kappa)$ is approximated by (5.3) (Lierke 1996), valid for $\kappa \ll 1$ (here $\kappa = 0.05$):

$$f(\kappa) = \frac{5}{6}\kappa\frac{3}{(2\kappa)^2}\left(\frac{\sin(2\kappa)}{2\kappa} - \cos(2\kappa)\right). \tag{5.3}$$

In order to delimit the phenomenon, we determined the transverse velocity U_p^{lim} beyond which droplets, initially located at a velocity anti-node, cannot go back to the

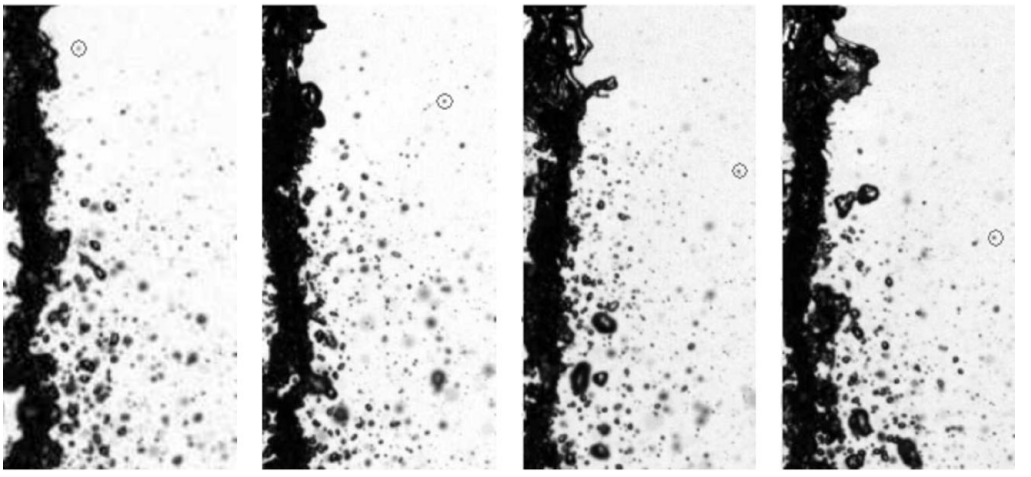

(*a*) t_0 (*b*) $t = t_0 + 13.5$ ms (*b*) $t = t_0 + 27$ ms (*d*) $t = t_0 + 40.5$ ms

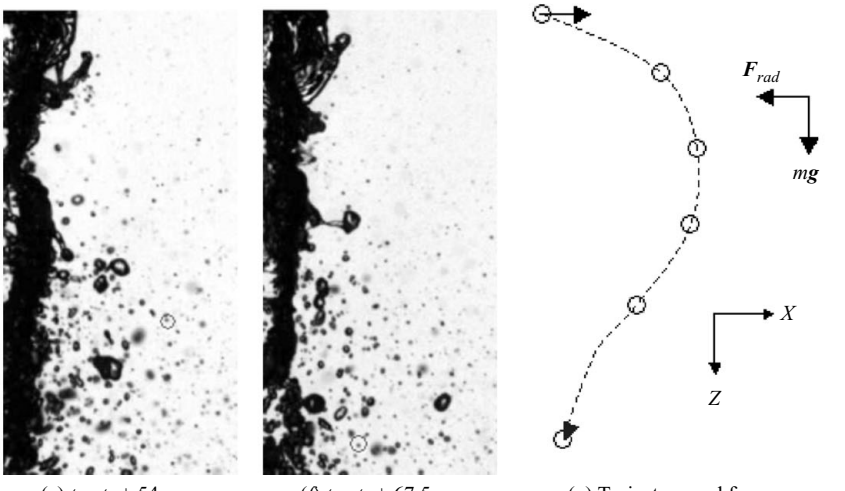

(*e*) $t = t_0 + 54$ ms (*f*) $t = t_0 + 67.5$ ms (*g*) Trajectory and forces

FIGURE 21. Front views showing the trajectory of a droplet initially located near a velocity anti-node. $We = 65$, $Re_l = 3536$, $P_{ac} = 3600$ Pa.

anti-node plane. Projecting the momentum equation applied to a droplet on to the $\boldsymbol{X}$ direction, we obtain the differential equation of a simple pendulum:

$$\frac{\partial^2 \xi}{\partial \tau^2} = -\sin(\xi) \tag{5.4}$$

with

$$\xi = \frac{4\pi}{L_c}\left(X - \frac{L_c}{4}\right) \tag{5.5}$$

and

$$\tau = t\sqrt{\frac{3k^2 P_{ac}^2}{2\kappa \rho_g \rho_l c^2} f(\kappa)}. \tag{5.6}$$

Four different behaviours are possible for the droplet, depending on the value of $(\partial\xi/\partial\tau)_{\tau=0}$ which is proportional to U_p^0.

For $(\partial\xi/\partial\tau)_{\tau=0}=0$, the droplet initially located at a velocity anti-node is not submitted to any lateral displacement, as $\boldsymbol{F}_{rad}$ is null for this position.

For $0<\|(\partial\xi/\partial\tau)_{\tau=0}\|<2$, the droplet is decelerated by the resulting radiation force pointed towards its initial position. The droplet velocity goes to zero before it can reach the next pressure anti-node located at either $X=0$ or $X=L_c/2$; $\boldsymbol{F}_{rad}$ imposes on the droplet an accelerating back movement towards its initial position. Theoretically, the droplet should periodically oscillate around its initial position. However, the droplet progressively moves towards the vertical descending direction under the action of its weight and of the gasdynamics. Figure 21 illustrates such a movement.

For $\|(\partial\xi/\partial\tau)_{\tau=0}\|>2$, the droplet is decelerated until it attains the nearest pressure anti-node plane. As the droplet reaches this plane with a non-null velocity, it passes through it and is accelerated in the same direction. The droplet thus continues to move away from its initial position, as $\boldsymbol{F}_{rad}$ is oriented the other way over the pressure anti-node plane.

For $\|(\partial\xi/\partial\tau)_{\tau=0}\|=2$, the droplet asymptotically goes towards the nearest pressure anti-node plane. This condition defines the limit velocity U_p^{lim}:

$$U_p^{lim}=\sqrt{\frac{3P_{ac}^2}{2\kappa\rho_l\rho_g c^2}f(\kappa)}. \tag{5.7}$$

Droplets having an initial transverse velocity U_{ini}^{trans} greater than U_p^{lim} cannot go back to the velocity anti-node. Droplets verifying $U_{ini}^{trans}<U_p^{lim}$ are brought back to the velocity anti-node, i.e. towards the liquid sheet. Since $\boldsymbol{F}_{rad}$ is oriented from pressure anti-nodes towards velocity anti-nodes, a segmentation of the spray can occur, droplets being gathered at velocity anti-node planes. As indicated by (5.7), the segmentation is particularly efficient for the smallest droplets of the spray. For the droplet followed in figure 21, U_p^{lim} is found to be of the order of $1.3\,\mathrm{m\,s^{-1}}$, which is greater than its own velocity. It is therefore obvious that this drop must return to the anti-node plane. Such a deviation was quantified and also interpreted as induced by the resulting radiation force by Carpentier *et al.* (2009) on a non-assisted cylindrical liquid jet placed between a pressure node and a pressure anti-node.

6. Concluding remarks

The action of a transverse acoustic field on the formation of a spray produced by an air-assisted atomizer has been studied. Jet regimes from the axisymmetric Rayleigh regime up to the fibre-type regime were exposed to the planar standing waves of an intense acoustic field (up to 3600 Pa of pressure fluctuations). The jet was placed at a pressure anti-node or at a velocity anti-node. The acoustic field and the coaxial two-phase flow were experimentally quantified. The particular behaviours of the jet (liquid core and drops) are discussed according to the action of the acoustics. The nonlinear acoustic effect of the radiation pressure explains some of the responses of the jet.

At the pressure anti-node, the effects on the liquid core are mainly due to the unsteady modulation of the annular gas flow induced by the acoustic waves provided that the mean dynamic pressure of the gas is lower than the acoustic pressure amplitude in the cavity. Indeed, the external adverse fluctuating pressure is able to decelerate or even stop the gas flow over a fraction of the acoustic period. During the

remaining time, the flow rate is increased and leads to the formation of a vortex. The gas vortices periodically emitted at the nozzle exit modify the liquid core behaviour. This feature is crucial for rocket engines, as some coupling can be expected between the vortex shedding and the longitudinal instabilities that can develop inside injectors, as proposed by Cheuret (2005) and Kim & Sohn (2007). Here, a modification of the liquid core shape is observed for jets initially in axisymmetric or non-axisymmetric Rayleigh regimes or in the shear breakup regime.

For the low acoustic levels, the jet is stabilized (its breakup length is increased) due to the symmetrization of the gas coflow. For higher acoustic levels, a shear stress instability appears at the liquid–gas interface and contributes to accelerating the breakup of the liquid jet. On the other hand, at such a location in the acoustic field, the radiation pressure has no effect on the liquid core. As given by the calculation based on King's theory, the radiation pressure field at the interface is almost constant and acts as a mean pressurizing environment; the resulting radiation force acting on particles placed at this pressure anti-node is null. But an increase of the spray angle is observed experimentally, probably related to nonlinear acoustics. Indeed, droplets of the spray can be accelerated from the pressure anti-node towards the velocity anti-nodes under the action of the radiation force, as soon as they are outside the vicinity of the injection axis.

At a velocity anti-node, two large-scale effects are noted. First, local nonlinear radiation pressure effects flatten the jet to form a liquid sheet, provided that initially the regime is not the fibre regime. This restriction is probably due to the fact that in our experiments, acoustic levels limited to 165 dB cannot counterbalance gas impulse. Second, the spray is also spatially organized under these conditions. Large liquid clusters and droplets with a low ejection velocity can be brought back to the velocity anti-node plane, under the action of the resulting radiation force.

A new criterion is proposed to predict the appearance of the jet flattening for all the flow conditions. It is based on an acoustic radiation Bond number that, unlike a traditional Bond number, takes into account the influence of the frequency. It extends to coaxial jets the purely acoustic approach, as long as a position along the liquid core can be found at which acoustic pressure amplitudes counterbalance the gas impulse. However, an extension of the criterion to the fibre regime might integrate the gas impulse, ρU_g^2.

Once the sheet is formed, it is rapidly atomized by three main phenomena: intrinsic sheet instabilities, Faraday instability and liquid membrane and cluster breakup. Each of them presents drop-size distributions with a characteristic range. The breakup length L_{bu} is greatly reduced compared to the lengths obtained without acoustics. For example, for $We > 60$, L_{bu} tends, from below, up to the length measured in the fibre-type regime. Globally, this process promotes atomization.

These results suggest that in rocket engines, because of the large number of injectors, a spatial redistribution of the spray could occur and lead to an increase in the drop concentration near the velocity anti-node locations, when the acoustic pressure inside the cavity cannot be counterbalanced by the fluids' dynamics. This is particularly crucial during the transitory phases when the nominal state is not yet been attained, since liquid jets and droplets of reactants persist. This could lead to inhomogeneous combustion resulting in high-frequency combustion instabilities.

We would like to thank the Centre National aux Etudes Spatial which supported this study through the R&T programme on High Frequency Combustion Instabilities in Liquid Rocket Engines and the region Haute-Normandie.

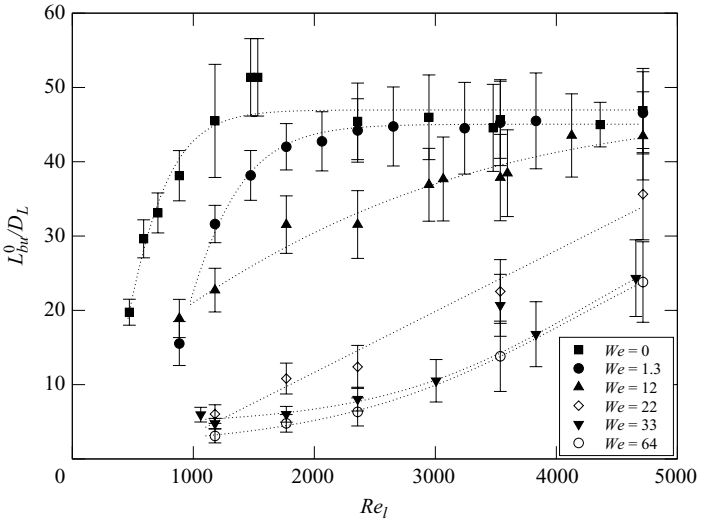

FIGURE 22. Reduced breakup length L^0_{bu}/D_l versus Re_l for different We.

Appendix A. Breakup length of the jet without acoustics

The breakup length of the jet, L^0_{bu}, is the distance between the nozzle exit plane and the extremity of the liquid core. Breakup length versus Re_l is reported in figure 22 for different values of the Weber number without acoustics. For jets in the axisymmetric Rayleigh regime ($We < 22$), L^0_{bu} increases with Re_l from $20D_l$ to $45D_l$, a value reached asymptotically with a concave curvature evolution. This particular behaviour is caused by the domination of the gravity effect leading to an acceleration of the jet and a reduction of the jet diameter along the downstream position. Indeed, the Froude number $Fr = (D_l/U_l)/\sqrt{D_l/g}$ (defined as the ratio of the convection time over the relaxation time due to gravity) ranges between 1 and 10, indicating that the jet responds to gravity more promptly than to convection. For $We \geqslant 22$, L^0_{bu} is of the order of $5D_l$ for low liquid Reynolds numbers and increases with Re_l, attaining the upper limit of $45D_l$ with a positive curvature. For $We = 22$, the evolution is almost linear.

A comprehensive and extended literature review on the jet core length of rocket-like injectors has recently been carried out by Davis & Chehroudi (2006). It analyzes experimental results and correlations obtained during these last decades. They cover a large range of conditions and of injection parameters; in particular single-phase and two-phase coaxial jets are considered as well as subcritical and supercritical thermodynamic conditions. The numerous results concerning the core length variations are summarized in figure 10 of their paper. From all these results, two typical trends are highlighted by the authors. For two-phase flow and/or subcritical conditions, function $J^{-0.2}$ fits non-dimensional core length data, whereas for single-phase flow and/or near-critical or supercritical conditions, function $J^{-0.5}$ fits them well. A similar representation of the present breakup length measurements is proposed in figure 23. Some correlations from the literature are also added in the figure, i.e. Lasheras & Hopfinger (2000) ($6/J^{0.5}$) and Davis & Chehroudi (2006) ($12/J^{0.5}$ and $25/J^{0.2}$). An additional curve ($24/J^{0.5}$), better correlated to our results, is also plotted. The two trends mentioned above are noted. Here, as long as small Weber numbers are considered (i.e. $We < 22$), the breakup length evolution is well fitted by

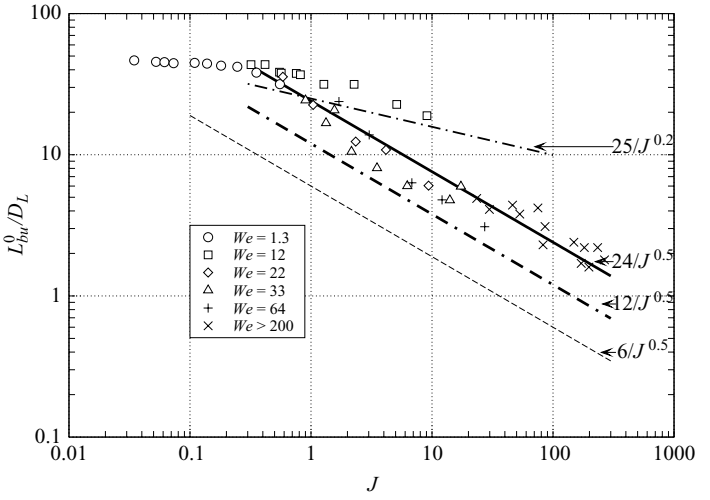

FIGURE 23. Reduced breakup length L^0_{bu}/D_l versus J.

the function $J^{-0.2}$, as underlined by Davis & Chehroudi (2006) for two-phase flows. For higher Weber number conditions, L_{bu} follows a momentum flux ratio dependence on $J^{-0.5}$, similar to the one reported by Davis & Chehroudi (2006) for single-phase jets or under supercritical conditions.

Appendix B. Radiation pressure field around a spherical particle

Let us consider a spherical droplet of radius R and centre G, placed in a standing wave directed in the $\boldsymbol{X}$ direction and characterized by its wavenumber k; $X = 0$ corresponds to a pressure anti-node and X_G to the position of G. Let M be a point placed on the surface of the sphere and ζ the cosine of the angle between the standing-wave direction $\boldsymbol{X}$ and vector $\boldsymbol{GM}$. The radiation pressure at the point M is given by

$$p_{rad}(\zeta) = \frac{P_{ac}^2}{4\rho_g c^2} g(\kappa, \tilde{X}_G, \zeta). \tag{B 1}$$

Here,

$$\begin{aligned} g(\kappa, \tilde{X}_G, \zeta) = \Bigg\{ &- \left[\left(\sum_{n=0}^{\infty} \frac{G_n}{H_n^2 \kappa^{n+2}} (2n+1) \cos\left(\frac{1}{2} n\pi + \tilde{X}_G \kappa \right) \frac{\mathrm{d}P_n(\zeta)}{\mathrm{d}\zeta} \right)^2 \right. \\ &\left. + \left(\sum_{n=0}^{\infty} \frac{F_n}{H_n^2 \kappa^{n+2}} (2n+1) \cos\left(\frac{1}{2} n\pi + \tilde{X}_G \kappa \right) \frac{\mathrm{d}P_n(\zeta)}{\mathrm{d}\zeta} \right)^2 \right] (1-\zeta^2) \\ &+ \left[\left(\sum_{n=0}^{\infty} \frac{G_n}{H_n^2 \kappa^{n+1}} (2n+1) \cos\left(\frac{1}{2} n\pi + \tilde{X}_G \kappa \right) P_n(\zeta) \right)^2 \right. \\ &\left. + \left(\sum_{n=0}^{\infty} \frac{F_n}{H_n^2 \kappa^{n+1}} (2n+1) \cos\left(\frac{1}{2} n\pi + \tilde{X}_G \kappa \right) P_n(\zeta) \right)^2 \right] \Bigg\}, \end{aligned} \tag{B 2}$$

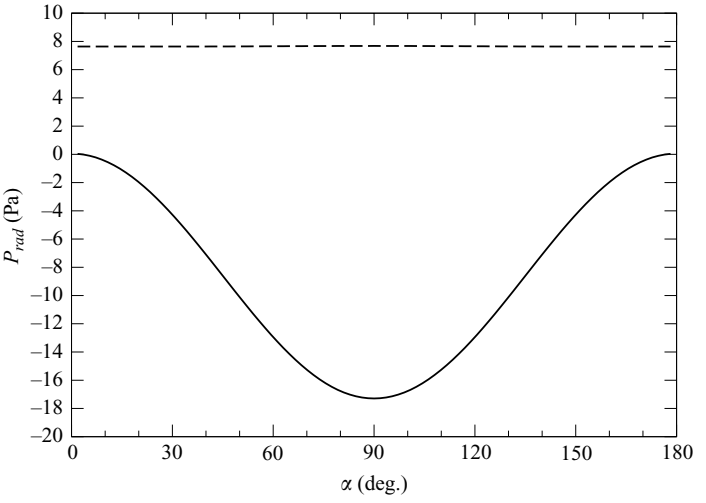

FIGURE 24. P_{rad} around the half-meridian of a sphere from equation B 2 for $\kappa = 0.055$ ($D_G =$ 6 mm, $f = 1000$ Hz), $P_{ac} = 2150$ Pa. —, at a velocity anti-node; - -, at a pressure anti-node.

where P_n are the Legendre polynomials, $\kappa = kR$, $\tilde{X}_G = X_G/R$:

$$\psi(n) = \kappa^{-n}\left(\frac{\pi}{2\kappa}\right)^{1/2} J_{n+1/2}(\kappa),$$

$$\phi(n) = (-1)^n \kappa^{-n}\left(\frac{\pi}{2\kappa}\right)^{1/2} J_{-n-1/2}(\kappa),$$

$$F_n = \kappa^2 \phi_{n+1} - n\phi_n,\ n \neq 1,$$

$$F_1 = \kappa^2 \phi_2 - \left(1 - \frac{\rho_G}{\rho_L}\right)\phi_1,$$

$$G_n = \kappa^2 \psi_{n+1} - n\psi_n,\ n \neq 1,$$

$$G_1 = \kappa^2 \psi_2 - \left(1 - \frac{\rho_G}{\rho_L}\right)\psi_1,$$

$$H_n = F_n^2 + G_n^2,\ \forall n.$$

Examples of radiation pressure distribution are given in figure 24 for the case of a sphere placed at either a velocity anti-node or a pressure anti-node. At a pressure anti-node, the radiation pressure is almost constant all around the sphere and simply acts as a mean pressurizing environment. At a pressure node, the radiation pressure presents a strong variation with a minimum negative value in the direction perpendicular to the acoustic axis, resulting in a dominant suction effect.

REFERENCES

ANDERSEN, O., HANSMANN, S. & BAUCKAGE, K. 1996 Production of fine particles from melts of metal or highly viscous fluids by ultrasonic wave atomization. *Part. Part. Syst. Charact.* **13**, 217–223.

ANDERSON, W. & YANG, V. 1995 *Liquid Rocket Engine Combustion Instability*, Progress in Astronautics and Aeronautics, vol. 169. AIAA, Academic Press.

ANILKUMAR, A. V., LEE, C. P. & WANG, T. G. 1993 Stability of an acoustically leviated and flattened drop. *Phys. Fluids* **A5** (11), 2763–2774.

Bauckage, K., Andersen, O., Hansmann, S., Reich, W. & Schreckenberg, P. 1996 Production of fine powders by ultrasonic standing wave atomization. *Powder Technol.* **86**, 77–86.

Boluriaan, S. & Morris, P. J. 2003 Acoustic streaming: from Rayleigh to today. *Intl J. Aeroacous.* **2** (3–4), 255–292.

Brenn, G., Prebeg, Z., Rensink, D. & Yarin, A. L. 2005 Control of spray formation by vibrational excitation of flat-fan and conical liquid sheets. *Atom. Sprays* **15**, 661–685.

Buffum, F. G. & Williams, F. A. 1967 Response of Turbulent Jets to Transverse Acoustic Fields. In *Proceedings of the 1967 Heat Transfer and Fluid Mechanics Institute* (ed. P. A. Libby, D. B. Olfe & C. W. Van Atta), pp. 247–276. Stanford University Press, Stanford, CA.

Cabeza, C., Gibiat, V. & Negreira, C. 2003 Observation of highly localized structures in a Faraday experiment with highly dissipative fluids. *Physica* A **327**, 34–38.

Candel, S., Huynh, C. & Poinsot, T. 1996 *Unsteady Combustion*. Kluwer Academic.

Carpentier, J. B., Baillot, F., Blaisot, J. B. & Dumouchel, C. 2009 behaviour of cylindrical liquid jets evolving in a transverse acoustic field. *Phys. Fluids* **21**, 023601-1–023601-15.

Chehroudi, B. & Talley, D. 2002 Preliminary visualizations of acoustic waves interacting with subcritical and supercritical cryogenic jets. In *15th Annual Conference on Liquid Atomization and Spray Systems (ILASS Americas)*, Madison, WI.

Cheuret, F. 2005 Instabilités thermo-acoustiques de combustion haute-fréquence dans les moteurs fusées. PhD thesis, University of Provence-Aix-Marseille I.

Davis, D. W. 2006 On the behaviour of a shear-coaxial jet, spanning sub- to supercritical pressures with and without an externally imposed transverse acoustic field. PhD thesis, Pennsylvania State University.

Davis, D. W. & Chehroudi, B. 2006 Shear-coaxial jets from a rocket-like injector in a transverse acoustic field at high pressures. In *44th AIAA Aerospace Sciences Meeting*, Reno, NV.

Faraday, M. 1831 On the forms and states of fluids on vibrating elastic surfaces. *Philos. Trans. R. Soc. Lond.* **52**, 319–340.

Farago, Z. & Chigier, N. 1992 Morphological classification of disintegration of round jets in a coaxial airstream. *Atom. Sprays* **2**, 137–153.

Gomi, H. 1985 Pneumatic atomization with coaxial injectors: measurements of drop sizes by the diffraction method and liquid phase fraction by the attenuation of light. *Tech Rep.* TR-888T. National Aerospace Laboratory.

Hager, F. & Benes, E. 1991 A summary of all forces acting on spherical particles in a sound field. In *Proceedings of the Ultrasonic International Conference*. Le Touquet, France, pp. 283–286.

Harrje, D. T. & Reardon, F. H. 1972 *Liquid Propellant Rocket Combustion Instability*, vol. NASA SP-194. NASA.

Hoover, D. V., Ryan, H. M., Pal, S., Merkie, C. L., Jacobs, H. R. & Santoro, R. J. 1991 Pressure oscillations effects on the jet breakup. *Heat Mass Transfer Spray Syst.* **187**, 27–36.

Hopfinger, E. J. 1998 Liquid jet instability and atomisation in a coaxial gas stream. In *Advances in Turbulence VII* (ed. U. Frich), pp. 69–78.

Hopfinger, E. J. & Lasheras, J. C. 1994 Breakup of a water jet in high velocity co-flowing air. In *Proceedings of the ICLASS 1994*. Rouen, France.

Ingebo, R. D. 1992 Effect of gas mass flux on cryogenic liquid jet breakup. *Cryogenics* **32** (3), 101–103.

Kim, H. & Sohn, C. H. 2007 Experimental study of acoustic damping induced by gas–liquid scheme injectors in a combustion chamber. *J. Mech. Sci. Tech.* **21**, 153–161.

King, L. V. 1934 On the acoustic radiation pressure on spheres. *Proc. R. Soc. Lond* A **147** (861), 212–240.

Landau, L. & Lifchitz, E. 1989 *Mécanique des Fluides*, ed. MIR, 1989.

Lang, R. J. 1962 Ultrasonic atomization of liquids. *J. Acous. Soc. Am.* **34**, 6.

Lasheras, J. C. & Hopfinger, E. J. 2000 Liquid jet instability and atomisation in a coaxial gas stream. *Annu. Rev. Fluid Mech.* **32**, 275–308.

Lee, C. P., Anilkumar, A. V. & Wang, T. G. 1991 Static shape and instability of an acoustically levitated drop. *Phys. Fluids* **A3** (11), 2497–2515.

Lee, C. P. & Wang, T. G. 1993 Acoustic radiation pressure. *J. Acous. Soc Am.* **94** (2), 1099–1109.

Lessmann, N. 2004 Numerical and experimental investigation of the disintegration of polymer melts in an ultrasonic standing wave atomizer. PhD thesis, Paderborn University.

Lefebvre, A. H. 1989 *Atomization and Sprays*. Hemisphere.

Lierke, E. G. 1996 Akustische Positionerung – Ein umfassender Ueberblick, ueber Grundlagen und Anwendungen. *Acta Acous.* **82** (220–237).

Marmottant, P. 2001 Atomisation d′un liquide par un courant gazeux. PhD thesis, University of Grenoble.

Mitome, H. 1998 The machanism of generation of acoustic streaming. *Electron. Comm. Jpn, Part 3* **81** (10), 1–30.

Oschwald, M., Smith, J. J., Branam, R., Hussong, J., Schik, A., Chehroudi, B. & Talley, D. 2006 Injection of fluids into supercritical environments. *Combust. Sci. Technol.* **178**, 49–100.

Otsu, N. 1979 A threshold selection method from grey scale histogram. *IEEE Trans. Syst. Man Cybernet.* **1**, 63–66.

Petit, L. & Gondret, P. 1992 Redressement d′un écoulement alternatif. *J. Phys. II* **2**, 2115–2144.

Raynal, L. 1997 Instabilité et entraînement à l'interface d'une couche de mélange liquide-gaz. PhD thesis, University of Grenoble.

Reipschläger, O., Bothe, D., Warnecke, H. J., Morien, B., Prss, J. & Weigand, B. 2002 Modelling and simulation of the disintegration process in an ultrasonic standing wave atomizer. In *ILASS-Europe 2002*, Saragossa, Spain.

Rey, C. 2004 Interactions collectives dans les instabilités de combustion haute fréquence. Application aux moteurs-fusées ergols liquides. PhD thesis, University of PARIS VI, Ecole Centrale Paris.

Sindayihebura, D., Cousin, J. & Dumouchel, C. 1997 Experimental and theoretical study of sprays produced by ultrasonic atomisers. *Part. Part. Syst. Charact.* **14** (2), 93–101.

Sujith, R. I. 2005 An experimental investigation of interaction of sprays with acoustic fields. *Exp. Fluids* **38**, 576–587.

Villermaux, E. 1998 Mixing and spray formation in coaxial jets. *J. Propul. Power* **14** (5), 807–817.

Vingert, L., Gicquel, P., Lourme, D. & Menoret, L. 1995 Coaxial Injector atomization. In *Liquid Rocket Engine Combustion Instability* (ed. V. Yang & W. Anderson), Progress in Astronautics and Aeronautics, vol. 169, pp. 145–189. AIAA.

Woods, D. & Lin, S. P. 1995 Instability of a liquid film flow over a vibrating inclined plane wave. *J. Fluid Mech.* **294**, 391–407.

Yarin, A. L., Pfaffenlehner, M. & Tropea, C. 1998 On the acoustic levitation of droplets. *J. Fluid Mech.* **356**, 65–91.